Translational energy dependence of Ar+ + XY→ArX+ + Y (XY = H₂,D₂,HD) from thermal to 30 eV c.m.

Kent M. Ervin and P. B. Armentrout[a]

Department of Chemistry, University of California, Berkeley, Berkeley, California 94720

Cross sections for the reactions of Ar^+ with H_2, D_2, and HD to form ArH^+ and ArD^+ are measured using a new guided ion beam tandem mass spectrometer which affords an experimental energy range from 0.05 to 500 eV laboratory. The apparatus and experimental techniques are described in detail. Cross sections for H_2 and D_2 are found to be nearly identical over this entire energy range when compared at the same barycentric energy. The total HD cross section is the same as H_2 and D_2 at low energies, but differs significantly above 4 eV c.m., where product dissociation becomes important. The intramolecular isotope effect for reaction with HD exhibits a reversal at low energy, favoring the deuteride product below ~0.14 eV c.m., and surprising nonmonotonic behavior at energies above 5 eV c.m. In all these systems, a new feature at higher energies is observed. This is interpreted as the onset of a product channel having an energy barrier of 8 ± 1 eV. The room temperature rate constant derived from the data for the reaction with H_2 is $(9.5 \pm 2) \times 10^{-10}$ cm^3 s^{-1}, in good agreement with the literature. Analysis of the data indicates an activation energy of between 2 and 15 meV at room temperature. The results are compared to previous experimental determinations and to theoretical reaction models.

I. INTRODUCTION

The hydrogen atom transfer reaction of argon(1+) ions with molecular hydrogen, reaction (1), and its deuterium analog, reaction (2),[1]

$$Ar^+ + H_2 \rightarrow ArH^+ + H, \quad \Delta H_0^o = -1.53 \pm 0.03 \text{ eV}, \quad (1)$$

$$Ar^+ + D_2 \rightarrow ArD^+ + D, \quad \Delta H_0^o = -1.50 \pm 0.03 \text{ eV}, \quad (2)$$

represent one of the most thoroughly investigated systems in the history of ion–molecule chemistry. Since the first experimental determinations of the reaction cross section by high pressure mass spectrometric methods in the midfifties,[2] increasingly sophisticated techniques have been used to probe the reaction kinetics and dynamics. These include determinations of the reaction rate,[3–11] integral reaction cross sections,[11–18] differential cross sections of reactive scattering,[19–23] velocity spectra of the products,[17,24,25] the intramolecular isotope effect,[12,17,26–28] and the state-selected reactions of the $^2P_{3/2}$ and $^2P_{1/2}$ electronic states of argon ions.[29,30] The related charge transfer reactions have also been investigated.[31–40]

For many years, it was presumed that exothermic ion–molecule reactions such as reactions (1) and (2) are dominated by the long range charge-induced dipole attractive potential. According to this view, the reaction rate should be near the close-collision rate given by the Langevin–Gioumousis–Stevenson (LGS) model.[41] Many experimental reaction rate and cross section results continue to be interpreted in terms of the LGS model and its refinements which include other terms in the long

range potential, viz. the charge-dipole and charge-quadrupole potential.[42,43]

More recently it has become recognized that crossings between low-lying potential energy surfaces are often important in determining the reactivity of ion–molecule systems. The rare gas ion–hydrogen reactions are cases in point. The analogs of reaction (1) for He^+ and Ne^+ are very exothermic, but there is no reaction at thermal energies.[44] In contrast, the reactions with Ar^+ and Kr^+ are much less exothermic, but have reaction rates in the vicinity of the LGS limit.[8] As discussed by Mahan,[45] these results can be qualitatively explained by electronic state correlations between reactants and products. Since XH^+ (X = He, Ne, Ar, Kr) dissociates to X and H^+, ground state products correlate with the asymptotic X–H_2^+ electronic state of reactants rather than with X^+–H_2. In a completely diabatic scheme, therefore, the X^+–H_2 entrance channel leads to a repulsive XH^+ excited state and is nonreactive. For reaction to occur, the reactants must reach the X–H_2^+ charge state which correlates to the XH^+–H exit valley as well as to charge transfer products. The relative energy levels of the X^+–H_2 and X–H_2^+ asymptotic states are fixed by the ionization potentials of the rare gas atom and H_2. In the cases of helium and neon, X^+–H_2 lies far above X–H_2^+. This prevents access to the potential energy surface leading to ground state products. Instead, a crossing with an excited, repulsive state of H_2^+ leads to dissociative charge transfer (but with low efficiency).

For the reactions of argon and krypton, in contrast, the energy levels of the two charge states lie close together and intersect near the H_2 equilibrium bond length. As the reactants approach, this intersection becomes avoided,
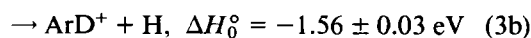
producing upper and lower adiabatic surfaces. This lower surface corresponds to the X^+-H_2 state at shorter H–H distances and to the X–H_2^+ state at longer H–H distances. The lower surface is attractive and leads adiabatically to XH^+ products. Reaction can easily occur either via adiabatic passage to the lower surface or via nonadiabatic transitions from the upper to the lower surface. In the reactions of argon ions with hydrogen, the interactions between the two entrance channel surfaces are particularly important because the asymptotic ground states are separated by only 0.33 eV.

Encouraging progress has been made in theoretical calculations of the nonadiabatic transitions between these two surfaces. Chapman and Preston[46] performed trajectory surface hopping (TSH) model calculations on diatomics-in-molecules with zero overlap (DIMZO) potential energy surfaces[47] for (Ar–H_2)⁺. Their calculations, which neglect spin-orbit coupling, indicate that of the three possible approaches corresponding to P_x, P_y, and P_z states, only the P_z approach of the reactants can reach the reactive surface. The P_z reactant state is quite reactive, but the TSH cross section is still less than half the LGS limit at the energy studied (3.36 eV c.m.). Baer and Beswick have performed quantum mechanical calculations of the nonadiabatic transitions probabilities for collinear reactions.[48] Their work indicates a barrier of ~0.06 eV for nonadiabatic transitions corresponding to an avoided crossing between the Ar⁺–$H_2(v = 0)$ and Ar–$H_2^+(v = 2)$ surfaces. Both these studies indicate that the two electronic state surfaces cross along a seam in the H_2 vibrational coordinate, implying a vibrational level specificity in the transition probabilities. A model by Tanaka et al.[29] used the DIMZO surfaces and included spin-orbit coupling, which mixes the P_x, P_y, and P_z states. The model predicts an enhancement of roughly $\sqrt{2}$:1 of the cross section for Ar⁺($^2P_{1/2}$) over Ar⁺($^2P_{3/2}$).

The available experimental evidence is only in partial agreement with these theoretical predictions. The reaction rate at 300 K is approximately two-thirds of the LGS rate[3–11] and the total reaction cross section has no apparent threshold.[11–18] The phenomenological cross section increases with decreasing energy to the lowest kinetic energy measured (0.01 eV c.m.)[14] at a rate slower than the LGS prediction but faster than Tanaka's model.[29] Threshold electron–secondary ion coincidence (TESICO) experiments for the state-selected reactions[29] show a 30% to 50% enhancement for the $J = 1/2$ state, in good agreement with the model. However, the TESICO results tend to refute a vibrational level specificity of the reaction probability.

Another area of theoretical interest in reactions (1) and (2) concerns the reaction dynamics and product energy distributions. Simple direct interaction models, particularly spectator stripping and various modifications thereof,[19–25,49] can account for the salient features of the experimental differential scattering cross sections and product velocity spectra for reactions (1) through (3), but no single model has accounted uniquely for all the details. Other approaches include hard-sphere sequential impulse models[50,51] and quantum mechanical collision dynamics.[52]

The intramolecular isotope effect in the reaction with HD,[1]

$$Ar^+ + HD \rightarrow ArH^+ + D, \quad \Delta H_0^\circ = -1.50 \pm 0.03 \text{ eV}, \quad (3a)$$

$$\rightarrow ArD^+ + H, \quad \Delta H_0^\circ = -1.56 \pm 0.03 \text{ eV} \quad (3b)$$

is particularly sensitive to assumptions made in these direct reaction models. Investigation of reactions (3a) and (3b), therefore, can provide insight into the reaction dynamics not attainable from reactions (1) and (2). In addition to the direct reaction models, an orientation model has been proposed to explain the low energy intramolecular isotope effect.[53]

In this work, reactions (1) through (3) are studied using a recently constructed guided ion beam tandem mass spectrometer. The apparatus is designed to allow accurate measurements of absolute integral cross sections of ion–molecule reactions as a function of the ion translational energy from 0.05 to 500 eV lab. The energy range and sensitivity of the guided beam instrument permits measurement of cross sections for reactions (1) through (3) at both higher and lower energies than previously reported. Results of several studies which utilized this apparatus have been published in brief, including the collision induced dissociation of Mn_2^+,[54(a)] reactions of Mn_2^+ with O_2,[54(b)] $C^+(^2P)$ with H_2,[54(c)] V⁺ with small hydrocarbons,[54(d)] and Si⁺ with H_2.[54(e)] In this work, we present a detailed discussion of the design, operation, and capabilities of the instrument as well as a comparison with other techniques.

II. EXPERIMENTAL TECHNIQUES

A. Overview

A schematic diagram of the guided ion beam tandem mass spectrometer is shown in Fig. 1. The basic experiment is simple in concept: a beam of ions of known mass and well-defined kinetic energy is allowed to react with neutral molecules under single collision conditions. All ionic reaction products are collected, mass analyzed, and detected. Absolute integral cross sections for individual product channels can then be determined as a function of the relative translational energy of the reactants.

Our apparatus is akin to the tandem mass spectrometers used in analytical chemistry, in which a mass-selected beam of ions passes through a static gas collision cell in a field-free region and fragmentation daughter ions are then mass analyzed.[55] Although conventional tandem mass spectrometers can be used for determining absolute reaction cross sections, their ability to make such measurements quantitatively is limited. This is because secondary ion collection efficiency depends strongly on the gas cell geometry and on the reaction dynamics, namely the direction in which the product ions are scattered. In the present apparatus, use of the ion beam guide technique[14] provides 4π collection of ionic products, permitting accurate quantitative measurements of integral cross sections of ion–molecule reactions. Another advantage of the beam guide is that it allows good energy resolution and operation at low nominal ion energies (down to 0.05
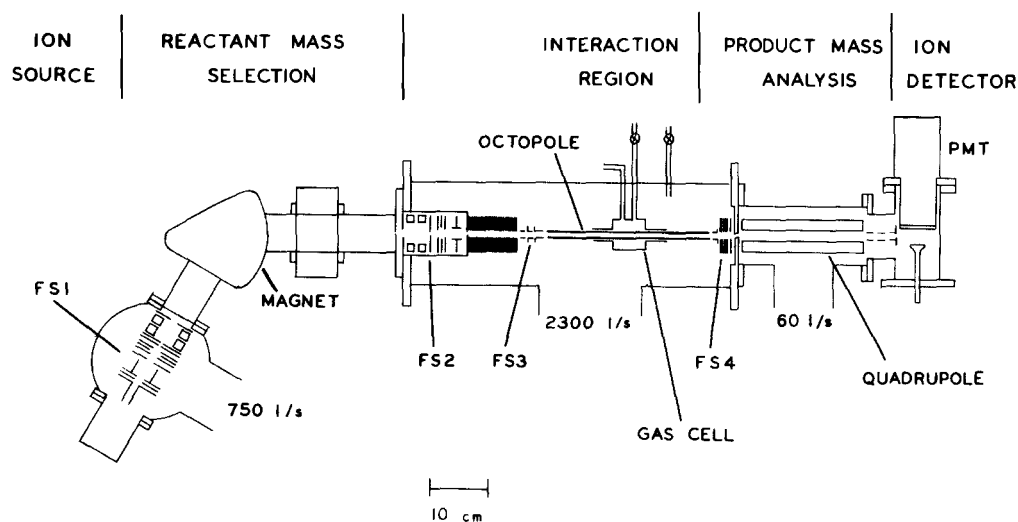
FIG. 1. Schematic overview of the guided ion beam tandem mass spectrometer.

eV lab). Thus, we are able to bridge the gap between determinations of ion–molecule reaction rate constants at room temperature and conventional ion beam experiments which are generally restricted to energies above one electron volt. Merged-beam techniques[56] are able to access these low energies also, but not on the routine experimental basis which the techniques described here afford. Drift/flow tube[57] and ion cyclotron resonance[58] can measure reaction rates at hyperthermal energies, but in those techniques the energy distributions are large or ill-defined.

B. Vacuum system

The vacuum system comprises three primary regions which are individually pumped: (1) the source chamber and magnetic sector flight tube, (2) the main chamber which includes the interaction region, and (3) the detector chamber. The source chamber is pumped by a 6 in. diffusion pump with a liquid nitrogen cooled cryotrap having an effective pumping speed of $\sim$750 l s^{-1}. A gate valve mounted on the flight tube (and biased at the mass analysis potential during operation) allows isolation of the source chamber for changing ion sources or for cleaning the ion lenses without venting the entire instrument. Despite frequent venting, the source chamber typically reaches a base pressure of $\sim$1 $\times$ 10^{-7} Torr ($\sim$1 $\times$ 10^{-5} Pa) within several hours. The source chamber lenses must be cleaned following the use of contaminating materials in the ion source, but otherwise the instrument can operate for months without requiring cleaning under normal conditions.

The main chamber is pumped continuously by a 2300 l s^{-1} diffusion pump with an integral water-cooled baffle (Edwards Diffstak model 250). The base pressure of the main chamber is $\sim$5 $\times$ 10^{-8} Torr ($\sim$6.5 $\times$ 10^{-6} Pa). The detector chamber, which contains the quadrupole mass filter and the ion detector, is differentially pumped by a 60 l s^{-1} ion pump (Varian VacIon).

C. Ion production

The ion source mating flange accepts several ion source units available in our laboratory. These include electron ionization sources with sample delivery via a gas inlet, a solid sample probe, or a sample oven; a surface ionization source with either a gas inlet or an oven; and a high pressure plasma (dc discharge) source. In the work presented here, argon(1+) ions are produced in a high efficiency electron ionization source similar in design to that of Udseth et al.[59] The gas to be ionized effuses from a molybdenum tube (1.0 mm inside diameter) which also serves as the anode. Electrons are produced at a resistively heated tungsten mesh filament placed perpendicularly in the beam line about 3 mm from the anode. The potential difference between the tungsten filament and the anode fixes the electron energy (E_e) and simultaneously creates a field which extracts the ions. The electron energy distribution is not well controlled, however, and its width may be as large as 2 eV. The nominal electron energy used for this study is 20 eV. The $^2P_{1/2}$ (0.17 eV) level of Ar$^+$ may be produced along with the $^2P_{3/2}$ (0.0 eV) state, presumably with a 33% statistical population. Higher excited states of Ar$^+$ are not present. The argon ion beam formed using this source has a translational energy distribution (as determined by methods described below) which is nearly Gaussian and has a typical full-width at half-maximum (FWHM) of 0.2 eV.

D. Ion beam formation

The ion beam formation optics are very similar to those used in a crossed beam apparatus built by Mahan and co-workers.[60] In focusing stage 1 (Fig. 1), ions are extracted from the source and collimated by a double aperture immersion lens, focused by an einzel lens, and then accelerated to the momentum analysis potential. Electrostatic quadrupole doublet lenses convert the beam from cylindrical symmetry to a ribbon shape appropriate for momentum analysis.

The magnetic momentum analyzer has been described by Gentry et al.[61] It consists of a magnetic sector with a 8 cm radius ion flight path and a 66° ion deflection angle. The magnet is asymmetric with an image distance of 12 cm and an object distance of 24 cm. This design produces an ion beam with a small angular divergence. The entrance and exit slit widths are 0.75 mm. The

analysis potential is typically 300 eV. Under these conditions, the momentum analyzer serves as a mass filter with a mass resolution of approximately 100 (m/Δm FWHM) for ions with an initial energy spread of less than 1 eV.

After the magnetic sector exit slit, the ion beam is reconverted to cylindrical symmetry by a second electrostatic quadrupole doublet lens and focused by an einzel lens (focusing stage 2, Fig. 1). A set of horizontal and vertical deflectors then center the beam on a 0.80 mm aperture, the entrance to the main chamber. Here the ions enter an exponential decelerator which is 10.2 cm long and consists of 33 evenly spaced plates. The decelerator plate potentials are determined by internally connected resistors except that the last four plates are tied together and are controlled externally. These last plates also constitute the first element of a set of lenses (focusing stage 3) which inject the ions into the ion beam guide. The measured angular divergence of the ion beam in a crossed-beam instrument with nearly identical beam formation optics is ~2° FWHM and the beam diameter is about 3 mm.[60] Refocusing by the octopole injection lenses, however, may alter these characteristics somewhat.

E. Octopole ion beam guide

Octopole ion beam guide techniques were pioneered by Teloy and Gerlich over a decade ago.[14] Since then octopole ion traps have found use in several other applications,[62] but have not been used extensively. The octopole is similar in concept to quadrupole traps which are in extensive use in analytical mass spectrometry (triple quadrupole MS/MS[63]). The beam guide is formed by eight rods placed in an octagonally symmetric array around the beam path. Radio frequency (rf) electric potentials applied in opposite phases to alternate rods produce an inhomogeneous field which creates an effective radial potential well. The octopole traps ions in radial directions over a broad range of ion masses while not affecting the axial ion velocities. The trapping insures that ionic products are collected regardless of scattering angle. The beam guide also allows operation at very low ion kinetic energies (<0.1 eV lab), where space-charge effects and spurious fields would disperse the ion beam in a conventional instrument.

The effective radial potential energy[64] for a hyperbolic multipole ion trap is given by

$$U_{eff}(r) = \frac{n^2 q^2 V_0^2}{4m\omega^2 r_0^2} \cdot \left(\frac{r}{r_0}\right)^{2n-2},$$ (4)

where $2n$ is the number of poles, q is the charge of the ion and m is its mass, r is the radial distance from the multipole axis, r_0 is the inner radius to the poles, and the rf potential applied to alternate rods is $\pm V_0 \cos(\omega t)$. The derivation of this effective potential is outlined in the Appendix. For an octopole ($n = 4$), the effective radial potential is proportional to r^6. This provides a large tubular trapping volume with low potential near the center and steep walls at a larger radius. These character-

istics result in very effective ion trapping with only small perturbations of the kinetic energies of ions traveling down the axis of the octopole. In comparison, the effective radial potential well of an rf-only quadrupole ($n = 2$) is proportional to r^2 and has a maximum trapping energy (at $r = r_0$) one-fourth that of the octopole, with other parameters held constant. This results in larger perturbations of ions near its axis and less efficient trapping. Thus, the octopole trapping field is more desirable than a quadrupole field for quantitative determinations of the energy dependence of cross sections.

Neutral reactants are introduced either in a collision cell which surrounds the octopole or in a molecular beam which crosses through it. In either case, ions produced in reactions taking place within the octopole are also trapped. As long as the secondary ions are scattered with a nonzero velocity in the forward beam direction, they will drift to the end of the octopole where they are extracted and detected. In cases where the reaction kinematics permit backward scattering in the laboratory frame, the ion beam can be pulsed and a repeller voltage placed on the entrance lens of the octopole immediately after the injection of the reactant ions. In this way, backscattered products are reflected back down the octopole and are eventually detected as well.

Figure 2 shows the construction details of the octopole, gas cell, and injection and extraction optics. The 30 cm long octopole consists of eight 0.8 mm diameter stainless steel rods held on an 11.1 mm diameter circumference. The rods are held in place by 1.6 mm diameter pins welded to the rods at each end; the weld joints are profiled and polished to preserve the symmetry of the octopole fields as much as possible. The optimal size and spacing of the octopole rods is dictated by several conflicting design considerations. First, the usable inside trapping area, perhaps half the free area between the rods, should match the ion beam size. Second, the outside diameter should be as small as possible in order to limit the gas conductance from the collision cell, through which the octopole must pass. Third, the lateral spacing between adjacent rods must be large enough to allow passage of
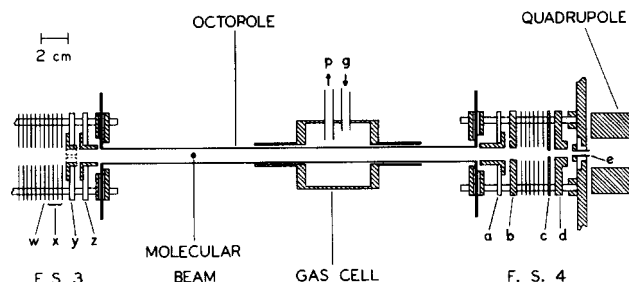

FIG. 2. Cross-sectional view of the octopole and interaction region. Focusing stage 3 (F.S. 3) consists of the end of the exponential retarder w and injection lenses x, y, and z. Lens y is split in two halves for use as a deflector to pulse the ion beam. Focusing stage 4 (F.S. 4) includes the extraction lens a, refocusing lenses b through d, and quadrupole injection lens e. The reactant gas enters the gas cell through inlet g or is introduced via a crossed molecular beam perpendicular to the plane of the page. The gas cell pressure is monitored by an external capacitance manometer via tube p.

the crossed molecular beam. Finally, the optimal rod radius would approximate that of an eightfold hyperbolic surface. The chosen geometry is a compromise among these considerations. The Appendix considers the effect of nonideal octopole geometry on the trapping efficiency. The source of the rf potentials is a sine-wave function generator (Tektronix FG502), stepped up to a maximum of 200 W by a rf power amplifier (ENI 2100L). This signal activates a resonant LC circuit consisting of the octopole rods and an induction coil located directly outside the vacuum chamber. The resonant frequency ($\omega/2\pi$) used is 6.8 MHz. The peak rf potential (V_0) on the rods can be varied up to 1000 V.

For reasons discussed in the Appendix, the trapping energy given by Eq. (4) for hyperbolic multipoles (with $r = r_0$) is higher than the actual value for nonideal multipoles. The actual beam guide trapping energy was calibrated using the reaction $Ar^+ + O_2 \rightarrow O_2^+ + Ar$, which has a large and known kinetic energy release.[65] The cross section at near-thermal energies was monitored as the applied rf potential was decreased. The point at which product collection started to fall off could then be related to the expected minimum trapping energy needed to trap the product ions. These experiments indicate that Eq. (4) gives trapping energies which are about an order of magnitude higher than the actual trapping energy.

The applied rf potential V_0 can be varied from 35 to 1000 V without a significant change in the primary ion beam intensity, although minor refocusing of the injection optics is necessary in the lower range. At rf potentials lower than $V_0 \approx 35$ V, the transmission is severely degraded for low ion energies. This minimum value of V_0 gives a trapping energy of ~0.25 eV according to Eq. (4), but taking into account the experimental calibration (above) this gives an actual trapping energy of about 25 meV. This corresponds to the expected magnitude of the ion beam transverse energy. The typical operating potential is $V_0 \simeq 500$ V, which provides a large margin of safety for complete trapping of secondary ions. In the present experiments and in all systems investigated on this instrument to date,[54] the experimental cross sections show no dependence on the octopole rf potential over large ranges. This indicates both that the secondary ions are efficiently trapped and that the rf potentials do not overly perturb the ion kinetic energies.

F. Injection and extraction optics

A critical aspect of the operation of the ion beam guide involves the transmission of ions through the entrance and exit regions of the octopole. Figure 2 shows the ion injection and extraction lenses, focusing stages 3 and 4, respectively. Ideally, all ions would enter at the center of the octopole field and would experience no net radial force. In practice, low energy ions and off-axis ions are easily deflected by fringing fields at the octopole entrance. To minimize this effect, the ions are strongly accelerated through the entrance and exit regions. A 16 mm long cylindrical injection lens (z) with an aperture diameter of 9.5 mm, slightly smaller than the octopole

diameter, is placed ~1.5 mm from the entrance end of the octopole rods. The ions are accelerated to 30 to 80 eV through injection lens z. Two additional lenses (x and y) provide transitional focusing between the end of the exponential decelerator (w) and the injection lens. Lens y is actually a split lens which can be used as a deflector to pulse the ion beam. Another cylinder lens (lens a in focusing stage 4) extracts the ions from the exit end of the octopole. This is biased at a high potential (~600 V) to insure efficient extraction of both primary and secondary ions. Lenses b through e refocus the ions and inject them into the quadrupole mass filter.

Another cause of ion losses is the presence of rf potentials on electrostatic ion lenses due to capacitive coupling with the octopole rods or rf feedthroughs. This problem is corrected by careful symmetrization of the rods and electrical connections, by balancing the rf phases, by rf shielding, and by liberal use of rf chokes to prevent feedback through ion lens power supplies. It is also found that the presence of dc electric fields due to grounded metal surfaces near the octopole can result in degradation of the ion beam focusing. Presumably, the relatively open geometry of our octopole allows deflection of ions within the octopole via the penetration of dc electric fields. This effect is eliminated by biasing the surfaces near the octopole at the octopole dc potential.

Constant ion beam intensity (within 5%) can be achieved over the entire energy range, 0 to 500 eV, by careful focusing of the injection and extraction optics. This makes feasible complete automation of ion energy scans.

G. Reactant gas introduction

Provision is made in the apparatus to introduce the neutral reactant either in a gas collision cell or a crossed molecular beam. Use of the molecular beam should reduce the energy broadening caused by the random thermal motion of the gas. The molecular beam mode of operation is still under development, however, and will be described elsewhere.

The gas cell (Fig. 2) consists of a 4.8 cm long × 4.8 cm diam main body with two attached 3.8 cm long × 0.72 cm diam tubes designed to limit the gas conductance from the cell. Gas is introduced to the cell via a leak valve (inlet g in Fig. 2). The collision cell pressure is measured using a capacitance manometer (MKS Baratron 310) outside the chamber and connected to the cell by a tube (p). The measured pressure is corrected for thermal transpiration.[66] The pressure profile along the octopole axis is approximately trapezoidal, with the pressure decreasing linearly from the measured value in the main cell body to zero at the ends of the attached tubes.[67] The effective cell length taking this profile into account is 8.6 cm ± 10%.

Pressures in the range of 0.03 to 1.0 mTorr (4 × 10⁻³ to 0.13 Pa) can be used for cross section measurements. The pressure is kept low enough to insure that secondary reactions are negligible. During operation, the main chamber background pressure is approximately 60

times smaller than the measured gas cell pressure. To provide a convenient way to measure background signals due to reactions outside the collision cell, the gas flow can be diverted directly into the main vacuum chamber instead of to the gas cell by switching remotely controlled electropneumatic valves on the inlet lines. In this configuration, the chamber background pressure is the same as when the gas is flowing to the collision cell.

The temperature of the gas cell is measured using a alumel/chromel thermocouple. The temperature is typically ~305 K, slightly elevated from ambient due to rf power dissipation by the octopole.

H. Ion mass analysis and detection

An ideal analyzer for product mass determination would provide unit mass resolution with 100% transmission for all masses and for ions with widely varying axial and transverse energies. If operated judiciously, the quadrupole mass filter can approach this ideal. The quadrupole rods and electronics are supplied by Extranuclear Laboratories. The rod diameter is 19 mm, the rod length is 22 cm, and a frequency of ~1.9 MHz is used. A relatively high analysis energy (30 to 100 eV) minimizes differences of transmission for product ions, which can be produced with varying energies. Transmission is also optimized by setting the resolution as low as is consistent with adequate separation of products. Measurements of the ion transmission indicate that these operating conditions can effectively eliminate mass discrimination effects for the primary beam over the mass range of 10 to 150 daltons. Alternatively, it is possible to operate at a higher resolution and apply mass discrimination corrections. We avoid this procedure whenever possible, however, because the transmission of secondary ions is dependent on the reaction dynamics as well as mass; operation at high quadrupole resolution might discriminate against strongly scattered or low energy products. In the present study, no mass corrections have been applied.

The apparatus utilizes a secondary electron scintillation detector of the Daly type[68] operated with an ion target potential of 25 to 30 kV. This device, combined with pulse counting electronics, has high counting efficiency and low mass discrimination. The scintillation photons are detected by a RCA 8850 photomultiplier tube. The unamplified output pulses of the photomultiplier are directly discriminated from noise (Tennelec model 453 discriminator) and counted using a scaler (Canberra model 2071) for digital data acquisition and a linear ratemeter (Tennelec model 526) for visual display. The counting response of the ion detection system is linear up to ~3 × 10⁷ s⁻¹ and the counting noise background is less than 5 s⁻¹, providing a dynamic range of over six orders of magnitude. A Faraday cup ion detector is built into the apparatus for diagnostic purposes. Although larger ion beam intensities can be used with the Faraday cup, the beam intensity is measured by pulse counting for cross section determinations to avoid possible systematic errors in the calibration of the analog signals relative to the ion counts.

I. Computer control

A Digital Equipment Corp. MINC-11 computer interfaces with the apparatus for control and data acquisition. The MINC is equipped with laboratory interfacing modules including digital-to-analog converters, analog-to-digital converters, digital logic outputs, a 10 MHz real-time clock and an IEEE-488 instrument communications bus. Under software control, the MINC utilizes the D/A's to fix the quadrupole mass setting and the interaction energy (via a Kepco BOP 100-1M programmable power supply). The minimum step sizes are 0.0125 dalton and 0.0125 eV, respectively. The reactant gas inlet valves are also computer controlled. The MINC collects the ion counts digitally from the scaler via the IEEE bus and also takes analog pressure readings from the capacitance manometer. FORTRAN programs have been developed which automate data collection and allow extensive signal averaging. The data are stored on floppy disks for later analysis.

J. Ion energy calibration

The potential difference between ion source anode and the interaction region (i.e., the dc level of the octopole) establishes the nominal laboratory ion kinetic energy, which can be varied from 0 to 500 eV. Operation at low ion energies requires accurate calibration of the energy scale. Depending on the ion source, the actual ion energy may differ by as much as several electron volts from the nominal laboratory energy. This variance arises from field effects in the ion source, from contact potentials, and from surface charge effects. We determine the kinetic energy of the reactant ions by two independent methods: retarding potential analysis and time-of-flight measurements.

The octopole beam guide itself serves as a highly efficient retarding energy analyzer. The ion beam intensity
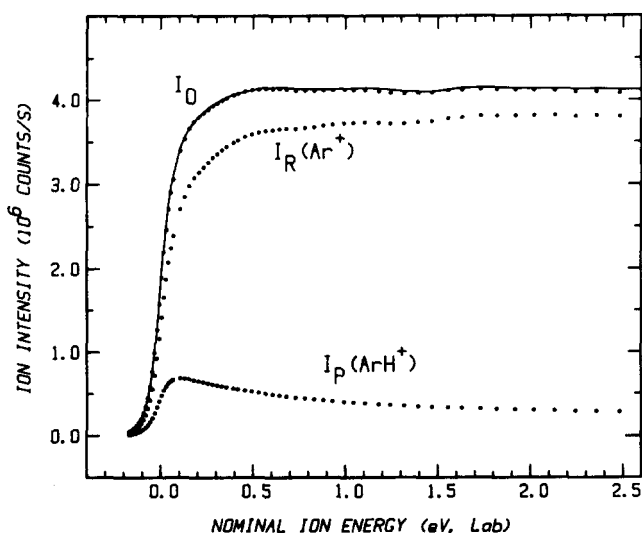

FIG. 3. Ion intensities for reaction (1) as a function of the laboratory ion energy. I_P is the ArH⁺ product ion intensity and I_R is the transmitted argon(1+) ion intensity. In the upper curve, the incident Ar⁺ beam intensity with no gas, I_0 (line), is compared to the sum of I_R and I_P (points). The H_2 gas pressure is 0.082 mTorr.
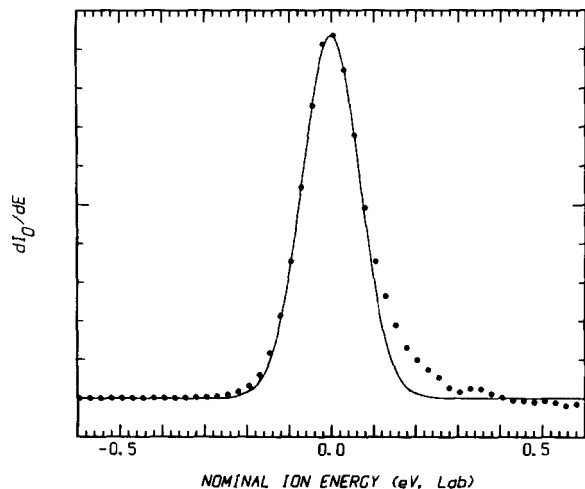
FIG. 4. Ion beam energy distribution obtained by taking the derivative of the retarding energy analysis curve. The solid line is a Gaussian curve fitted to the data points.

I_0 is observed as the dc voltage of the octopole is swept through the ion energy zero, producing a retardation curve such as that shown in Fig. 3 (solid line). The trapping characteristics of the octopole prevents dispersion of low energy ions due to space charge, a common problem in parallel grid retarding analyzers.[69] Since reactions take place in the same region as the energy analysis, there is no ambiguity in the interaction energy determination due to contact potential differences. The derivative of the retardation curve gives the ion energy distribution. A typical derivative curve is shown in Fig. 4 (points). The peak of the derivative curve, which can be determined with a precision of ±0.02 eV, is taken as the energy scale origin.

A pulsed ion beam mode of operation is used to perform time-of-flight (tof) measurements. The ion beam is pulsed on at deflector lens y (Fig. 2) by a high voltage pulse generator (Hewlett Packard model 214B), which simultaneously starts the MINC's real-time clock. After a software-controlled delay period (in microsecond increments), the clock triggers a gating pulse to the ion scaler. The ion pulse and counting gate widths are typically 10 μs. The cycle is repeated every 1 to 5 ms until the scaler has accumulated counts for a predetermined time (usually 0.01 s). The delay time is then incremented and the procedure is repeated until a tof distribution is obtained. The peak of the tof distribution can be determined with an uncertainty of ±1 μs. The tof determination is repeated at several energies to find an average energy scale origin.

The energy scale origin can be determined to within ±0.15 eV by the tof procedure. The determination of the energy zero by the time-of-flight method agrees with the retarding potential analysis to within this uncertainty, but the former tends to give results showing slightly higher ion energies (by ~0.1 eV). Teloy and Gerlich,[14] using a multichannel scaler with much better resolution (0.1 μs) for tof measurements, found the two methods agreed exactly. Since our tof arrangement is experimentally tedious and somewhat imprecise, only the retarding potential analysis method is used to determine the ion

energy for routine cross section measurements. We estimate our energy determinations have an overall uncertainty of ±0.05 eV lab. Our confidence in the energy calibration is bolstered by the close agreement of reactions (1) and (2) at the same barycentric energy despite very different laboratory energies (see results section). An energy error of just 0.1 eV would result in gross deviation of the two cross sections at low energies.

K. Ion energy distributions

For most ion sources the experimental primary ion energy distribution, as determined by the retarding energy analysis, is nearly Gaussian. A Gaussian curve fitted to the experimental distribution from the retarding energy analysis is shown in Fig. 4; the fit is good except for a small tail corresponding to slow ions. This tail is probably due to ions formed slightly away from the anode in the electron ionization source. The apparent FWHM from the retardation curve adequately describes the width of the Gaussian fit.

At the very low energies in the fall-off region of the retarding energy analysis curve, the slower ions are truncated from the distribution. This produces a narrowing of the ion energy distribution at these low energies. We take advantage of this effect to extend the energy range for cross section measurements to below one FWHM of the beam energy spread. Assuming the distribution is Gaussian with the FWHM found from the retarding potential analysis curve, the mean laboratory ion kinetic energy is given by

$$\bar{E}_{\text{lab}} = \frac{\int_0^\infty E \cdot P(E, E_{\text{lab}}) \cdot dE}{\int_0^\infty P(E, E_{\text{lab}}) \cdot dE}, \tag{5}$$

where $P(E, E_{\text{lab}})$ is a Gaussian distribution of ion kinetic energies E centered at a measured laboratory energy E_{lab} (which may be negative). The distributions obtained by time-of-flight measurements at these energies support this procedure, although the tof distributions indicate that the truncation of the Gaussian distribution is not perfectly sharp as assumed in Eq. (5). Rather, the truncation occurs over a range of ~0.05 eV. For this reason and because the distribution is not perfectly Gaussian, energies quoted which are smaller than one FWHM of the ion beam energy distribution (here ~0.2 eV lab) have larger uncertainties than higher energies.

The retarding potential analysis and tof methods measure only the axial energy of the ion beam energy. The transverse component of the ion energy must also be considered. Teloy and Gerlich[14] have shown that the transverse energy distribution of ions in the beam guide is strongly peaked at the initial value when the ion enters the octopole. A small percentage of the time, however, the transverse energy differs from the initial value due to oscillations of the rf field. This leads to variations from zero up to three times the initial value. The initial transverse energy can be estimated by considering the

angle of injection into the octopole. The transverse energy component will be on the order of $\sin^2(\alpha) \cdot E$ where α is the injection angle and E is the injection energy. The ion beam has an angular divergence of about $2°$ FWHM and the injection lens (z) is typically 30 to 80 V. Assuming a Gaussian distribution of injection angles, this gives most probable transverse energies of 9 to 23 meV. Measurements of the ion beam transmission as a function of the octopole trapping potential (Sec. II E) indicate the ion beam transverse energies are less than ~ 25 meV. In these studies, we take no explicit account of the transverse energy component except to include it in the overall uncertainty.

III. DATA ANALYSIS

A. Determination of cross sections

The experimental total reaction cross section, σ_{tot}, is determined by the relation

$$I_R = (I_R + \sum I_P)\exp(-\sigma_{tot}nl), \tag{6}$$

where I_R and I_P are the measured transmitted intensities of the reactant and product ions, respectively, n is the gas density, and l is the effective path length. Individual product cross sections σ_P are found by the formula

$$\sigma_P = \sigma_{tot} \cdot (I_P / \sum I_P). \tag{7}$$

Equations (6) and (7) presume that the sum of transmitted primary and secondary ions is equal to the incident ion intensity, i.e., $I_0 = I_R + \sum I_P$. Due to the 4π collection characteristics of the octopole, this is valid as long as all significant product channels are monitored. Figure 3 shows a plot of primary and secondary ion intensities for reaction (1) and compares their sum to the ion beam transmission without reactant gas. The H_2 gas cell pressure is 0.082 mTorr (0.011 Pa). Despite the greater than 10% attenuation of Ar^+ at the lower energies, the total ion collection is excellent. This is demonstrated by the agreement of the incident intensity and summed transmitted intensities.

1. Pressure dependence

In order to obtain a more accurate value of the reaction cross section, the reaction may be carried out at a number of pressures. For low pressures, Eqs. (6) and (7) reduce to the thin target limit:

$$I_P/I_0 = I_P/(I_R + \sum I_P) = \sigma_P nl. \tag{8}$$

Thus, at low pressures, the slope of the intensity ratio I_P/I_0 vs the gas density yields the product cross section. Figure 5 shows such a plot for reaction (1) at 0.50 eV. The intensity ratio is linear over the full pressure range shown, but curves downward above about 0.5 mTorr due to excessive attenuation of the ion beam and/or secondary reactions. The cross section for reaction (1) derived from the data in Fig. 5 is $(16.9 \pm 0.3) \times 10^{-16}$ cm^2.
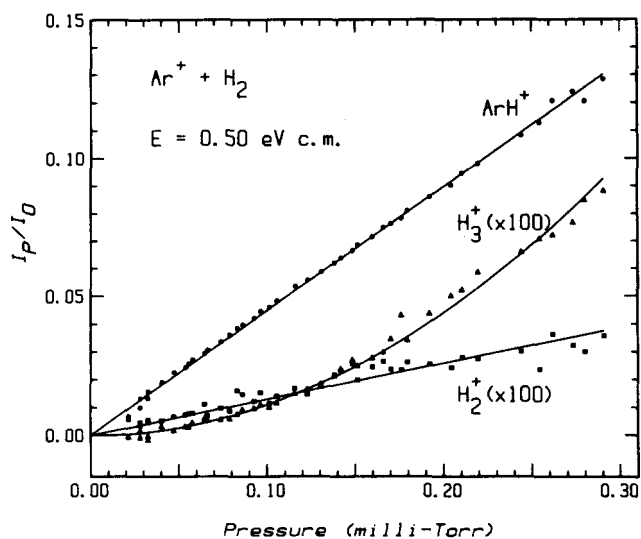

FIG. 5. Ratio of product ion intensity to incident ion intensity, I_P/I_0, as a function of the gas cell pressure for reaction (1) at an energy of 0.50 eV c.m. The H_2^+ and H_3^+ plots are magnified by a factor of 100. The lines through the data are linear for ArH^+ and H_2^+ and quadratic for H_3^+, the dependence expected for a secondary product ion.

2. Competing reactions
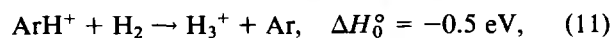
Figure 5 also shows the pressure dependence of the ion intensities for the H_2^+ charge transfer product, formed by reaction (9):

$$Ar^+ + H_2 \rightarrow H_2^+ + Ar, \quad \Delta H_0^\circ = -0.33 \text{ eV}. \tag{9}$$

This charge transfer process is near-resonant and can result in backscattered products in the lab frame.[32] Special precautions, namely pulsing the ion beam and placing a repeller voltage on the entrance of the octopole, are necessary to ensure complete collection of such products. This was not done when acquiring the data in Fig. 5, so the absolute cross section depicted for reaction (9) is low.

In cases where all product channels are not monitored, Eqs. (6) and (7) are still valid if the incident ion intensity is not significantly attenuated by the neglected channel, i.e., $I_{P'} \ll I_R$. The charge transfer product channel has a cross section of $(2-20) \times 10^{-16}$ cm^2 over the energy range examined.[29,33-40] To insure that the charge transfer process is negligibly small, pressures of hydrogen in the gas cell are kept below 0.15 mTorr (0.020 Pa) for this study. Therefore, the measurement of the cross sections for reactions (1) through (3) is not affected by the charge transfer reaction.

The secondary product H_3^+ may be formed by reactions (10) and (11),

$$H_2^+ + H_2 \rightarrow H_3^+ + H, \quad \Delta H_0^\circ = -1.7 \text{ eV}, \tag{10}$$

$$ArH^+ + H_2 \rightarrow H_3^+ + Ar, \quad \Delta H_0^\circ = -0.5 \text{ eV}, \tag{11}$$

each of which is exothermic and fast.[70] The H_3^+ intensities exhibits the quadratic dependence on pressure which is expected for a secondary process (Fig. 5). Since the intensity of this secondary product is more than 100 times smaller than the ArH^+ product intensity at the pressures used in the experiments, it has no significant effect on the measured cross sections.

3. Background corrections

Several sources of noise and background signals exist in these experiments and must be considered if accurate cross sections are to be obtained. First, there is random detector counting noise. The average counting noise (<5 s^{-1}) can be measured and directly subtracted from raw ion intensities. This counting noise is negligible except in measurements of the smallest cross sections—for example, near the threshold of endothermic reaction channels. Second, a background signal results when complete mass separation is not achieved between adjacent primary and secondary mass peaks. While it is instrumentally possible to separate the peaks completely, it is sometimes advantageous to use a lower quadrupole resolution in the interest of complete product transmission. Since the mass peak shapes are constant at a fixed quadrupole resolution, the signal due to the primary ion at the product mass setting can be determined without reactant gas and subtracted from the product mass signal obtained with gas.

The third type of background arises from reactions occurring outside the collision cell. This background is measured by directing the flow of reactant gas into the main chamber as described earlier. While the background pressure is a factor of 60 smaller than the gas cell pressure, the path length is quite long, resulting in an experimental signal to background ratio of about 15. Most of the background comes from the gas cloud outside the gas cell apertures but still in the octopole where the interaction energy is well defined. In all systems investigated to date, this background reaction signal has an energy dependence which is identical to the signal due to reaction in the gas cell. Thus, correcting for this background affects only the absolute value of the cross section and not the relative values as a function of energy—in effect a change in the effective gas cell length.

A practical way to correct for all three types of background signals simultaneously is to follow each energy scan taken with gas in the collision cell by an identical scan taken with the gas directed to the main chamber. The intensities from the background scan are then subtracted directly from the product intensities.

4. Sensitivity

The ultimate theoretical sensitivity limit for this apparatus is $\sim 1 \times 10^{-21}$ cm^2, based on the largest measurable reactant intensity ($\sim 3 \times 10^7$ s^{-1}), the smallest measurable product intensity (conservatively 10 s^{-1}), and a gas pressure of 1.0 mTorr. This estimate also assumes that the primary and secondary masses are well separated so that large background subtractions are not necessary. In practice, we have measured cross sections near the thresholds of endoergic reactions as small as 5×10^{-20} cm^2 with signal-to-noise ratios of greater than 5. For many systems of interest, the primary limitations on sensitivity are the ability to make ions beams of high intensity and the existence of secondary reactions which force the use of low gas pressures.

5. Precision and accuracy

The independence of the experimental cross section on various instrumental parameters over broad ranges is periodically checked to verify that the instrument is functioning properly and that product ions are being efficiently collected. These parameters include the octopole trapping voltage, extraction focusing potentials, primary beam intensity, and the quadrupole resolution and analysis energy. Cross section measurements are also repeated over a period of weeks or months. Based on the reproducibility of the results, the relative uncertainty of cross sections at different energies is within 5% for cross sections greater than 1×10^{-17} cm^2 and is limited by statistical counting uncertainties for smaller cross sections. The absolute accuracy of cross sections is limited mainly by our ability to measure the collision cell pressure and to estimate the effective path length. While this instrument has excellent collection efficiency characteristics, the possibility of secondary ion detection losses cannot be ruled out entirely. We estimate that the error in the absolute cross sections from all sources is within ±20%.

B. Interaction energy

1. Center-of-mass energy

Since the energy of the motion of the center-of-mass of the colliding reactants is not available for chemical change, the relevant energy for analysis of the results is the relative energy in the center-of-mass frame (E_0). Under the assumption of a stationary target molecule, E_0 is related to the laboratory ion kinetic energy according to the formula

$$E_0 = E_{\text{lab}} \cdot m_{\text{BC}}/(m_{\text{A}} + m_{\text{BC}}), \tag{12}$$

where m_{A} is the ion mass and m_{BC} is the target molecule mass.

2. Energy broadening

The random thermal motion of the reactant molecules in the gas cell creates a distribution of interaction energies for a given nominal ion energy. This so-called Doppler broadening effect has been discussed by Chantry,[71] who showed that the distribution is given by

$$f(E, E_0) = (1/4\pi\gamma k_B T E_0)^{1/2}$$
$$\times \{\exp[-(1/\gamma k_B T) \cdot (E^{1/2} - E_0^{1/2})^2]$$
$$- \exp[-(1/\gamma k_B T) \cdot (E^{1/2} + E_0^{1/2})^2]\}, \tag{13}$$

where E is the actual relative energy, E_0 is the nominal center-of-mass energy given by Eq. (12), $\gamma = m_{\text{A}}/(m_{\text{A}} + m_{\text{BC}})$, k_B is the Boltzmann constant, and T is the target gas temperature. The mean energy of this distribution is given by $\langle E \rangle = E_0 + (3/2)\gamma k_B T$. As a result of the energy distribution, the observed cross section as a function of the ion energy, $\sigma_{\text{eff}}(E_0)$, differs from the true cross section as a function of the relative interaction energy $\sigma(E)$. Chantry[71] derived the form of the convolution of $\sigma(E)$ for the case of a monoenergetic ion beam:

$$\sigma_{\text{eff}}(E_0) = \int_0^\infty (E/E_0)^{1/2} \cdot f(E, E_0) \cdot \sigma(E) \cdot dE. \quad (14)$$

The $(E/E_0)^{1/2}$ factor in Eq. (14) accounts for the difference in the residence times of ions in the interaction region at different nominal ion energies.

The Doppler broadening can partially obscure some features of the true excitation function, especially at low ion energies. Since the ion beam guide technique permits very low ion energies, it is important to evaluate the effect of the energy distributions. In Fig. 6, the energy distributions $f(E, E_0)$ are plotted for several center-of-mass energies (E_0) over the range of our experiments. The distributions have been normalized to unity at the most probable energy for ease of comparison. At high ion energies, $E_0 \gg k_B T$, the distributions are relatively narrow though much broader than that introduced by the ion beam energy spread. The distributions peak at $E \approx E_0$ and have a width given approximately by[71]

$$\text{FWHM} \approx (11.1\gamma k_B T E_0)^{1/2}. \quad (15)$$

The energy distributions at high ion energies may broaden sharp features in $\sigma(E)$, such as the threshold of an endoergic reaction channel, but are not sufficiently wide to obscure the overall behavior of the excitation function.

At low energies, the distribution function becomes broader relative to the center-of-mass ion energy. This corresponds to the breakdown of the stationary target approximation at energies where the velocities of the gas molecules are comparable to or larger than the ion velocity. In the limit of very slow ions, the relative velocity distribution is Maxwell–Boltzmann with an effective temperature $T' = \gamma \cdot T$. Thus, at the lowest ion energies accessible by the present apparatus, there is essentially a thermal distribution of translational energies. Figure 6 also shows Maxwell–Boltzmann energy distributions at 290 K [T' for reaction (1) when $T = 305$ K] and 50 000 K for comparison. It should be emphasized, however,

that the ions are *not* in thermal equilibrium. In the rarified environment of the gas cell, the ions pass through without undergoing enough collisions to become thermalized either translationally or internally. Rather, at these very low ion energies, the interaction energies are determined primarily by the thermal velocities of the target gas molecules. At intermediate energies, $k_B T < E_0 < 1$ eV, the effective energy distributions are relatively broad but are narrower than thermal.

3. Deconvolution

It would be desirable to extract the true excitation function behavior from the observed Doppler-broadened cross section. Unfortunately, direct deconvolution of the phenomenological cross section, $\sigma_{\text{eff}}(E)$, does not result in a unique form for $\sigma(E)$.[72] In order to infer the functional form of the true cross section, we customarily convolute a trial function for $\sigma(E)$ with the experimental energy distributions. The convoluted function can then be compared with the data. For this purpose, we use either Chantry's convolution [Eq. (14)] or the treatment of Tiernan and co-workers,[73] which includes the effect of the ion beam energy spread. Doppler broadening, however, dominates the broadening due to the ion beam energy width in the present experiments.

Use of this convolution and least-squares fitting procedure to infer the true cross section is relatively unambiguous when $E_0 \gg k_B T$. It has been used extensively to analyze the thresholds of endothermic ion–molecule reactions.[73,74] For $E_0 < k_B T$, however, the phenomenological cross section $\sigma_{\text{eff}}(E_0)$ is not very sensitive to the functional form of $\sigma(E)$, but rather is dominated by the $(1/E_0)^{1/2}$ term in Eq. (15). This means that the observed cross section tends toward $\sigma_{\text{eff}} \propto (E_0)^{-0.5}$ as $E_0 \to 0$ regardless of the low energy behavior of the true cross section. There may be a number of functions which when convoluted can reproduce the observed behavior. In such cases it is still possible to set limits on the functions $\sigma(E)$ which are consistent with the experiment.

C. Reaction rates

To compare the present results to experiments which measure the kinetic energy dependence of reaction rates, such as in flow/drift tube and ICR experiments, the cross sections must be converted into rate constants. The phenomenological rate constant is given by

$$k(v_0) = v_0 \cdot \sigma(v_0), \quad (16)$$

where $v_0 = (2E_0/\mu)^{1/2}$ is the nominal relative velocity of the reactants and $\mu = m_A m_{BC}/(m_A + m_{BC})$ is the reduced mass of the reactants. The rate $k(v_0)$ has the property that as $v_0 \to 0$ it approaches the thermal rate constant for the effective temperature $T' = \gamma \cdot T$. Since the beam guide technique allows very low ion energies, the rate constant at near room temperature can be obtained directly from the data at the lowest energy.

True thermal rate constants as a function of temperature are obtained by averaging the cross section over a Maxwell–Boltzmann distribution of relative energies:
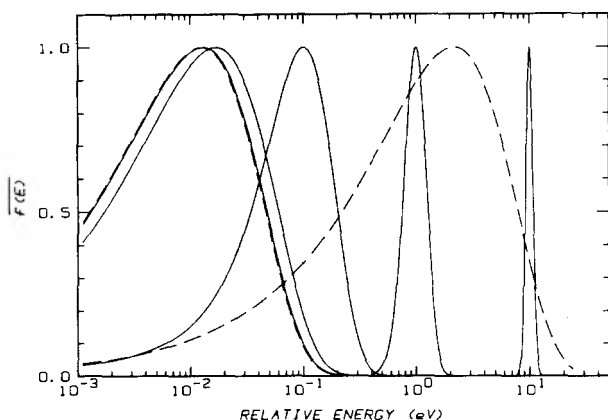

FIG. 6. Relative energy distributions due to Doppler broadening for reaction (1). All distributions are normalized to unity at the most probable energy. The solid curves show the experimental relative energy distributions according to Eq. (13) for ion energies of 0.001, 0.01, 0.1, 1.0, and 10.0 eV c.m. (left to right). The broken curves show thermal Maxwell–Boltzmann energy distributions at $T = 290$ K and $T = 50\,000$ K for comparison. The thermal distribution at 290 K is identical to the Doppler distribution in the limit of zero ion energy.

$$k(T) = (1/\pi\mu)^{1/2} \cdot (2/k_B T)^{3/2}$$

$$\times \int_0^\infty \sigma(E) \cdot E \cdot \exp(-E/k_B T) \cdot dE. \qquad (17)$$

Since only the translational energy of the reactants is varied in these experiments, the result is actually $k(T_k)$, the rate constant as a function of translational temperature. Thermal rate constants are obtained by direct numerical integration of the cross section data according to Eq. (17). The energy range of the present results corresponds to translational temperatures from ~300 to ~50 000 K. For temperatures above about 1000 K, the Maxwell–Boltzmann distributions are large relative to the Doppler energy distributions for the ion energies which contribute to reaction rate (cf. Fig. 6). Therefore, use of the phenomenological cross section in Eq. (17) instead of the true cross section does not greatly affect the calculated rate at high temperatures. At lower temperatures, however, the Maxwell–Boltzmann distributions are comparable to the Doppler distribution (Fig. 6), so the phenomenological cross section is not a reasonable approximation to $\sigma(E)$. Accurate determination of the thermal reaction rate at low temperature is possible only to the extent that the true cross section can be established.

IV. RESULTS

A. Ar⁺ + H₂, D₂

Figures 7 and 8 display the cross sections for reactions (1) and (2), respectively, as a function of the argon ion kinetic energy. Over the four orders of magnitude in energy we have measured (0.05 to 500 eV lab), the cross sections also vary by four orders of magnitude—from nearly 2×10^{-14} cm² at the lowest energy to 1×10^{-18} cm² at the highest. The center-of-mass energy scales in the plots are those calculated according to the stationary
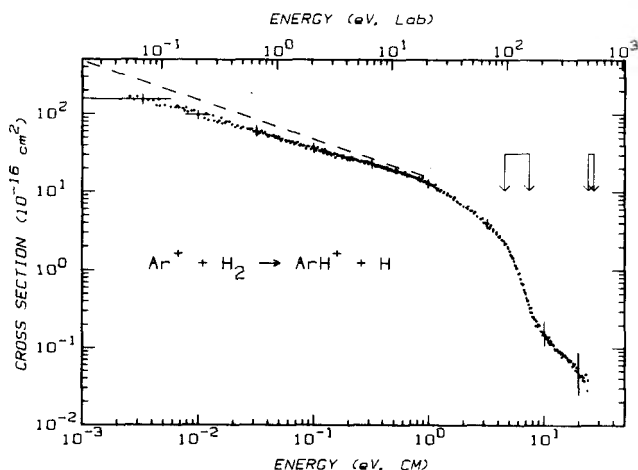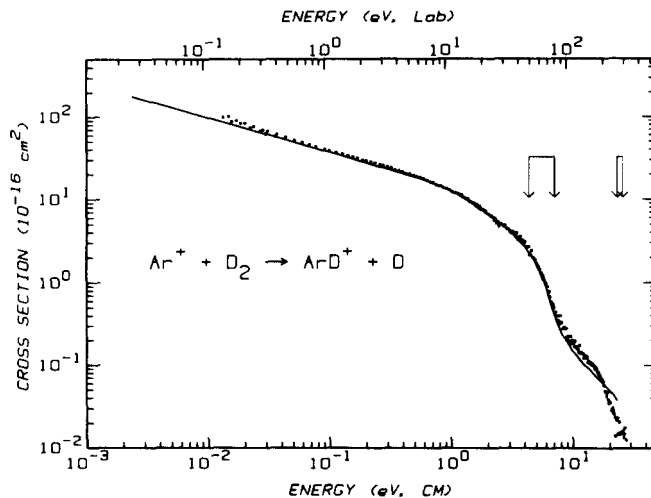

FIG. 8. Cross section for reaction (2) as a function of the argon ion kinetic energy in the laboratory frame (upper scale) and the center-of-mass frame (lower scale). Each point represents the average of several determinations; relative uncertainties are similar in magnitude to those given in Fig. 7 for reaction (1). The solid curve is a representation of the data for reaction (1) for comparison. The arrows indicate the critical energies, Table II, for product dissociation according the simple direct reaction models discussed in the text. From left to right, the arrows indicate E_S, E_R, E_S^*, and E_R^*.

target approximation, Eq. (12). (All further references to energy are in the center-of-mass frame unless otherwise noted.) The data are averages of results obtained in a number of determinations over a period of six months. The vertical error bars in Fig. 7 indicate ±2 standard deviations. The standard deviations are larger at the highest energies due to the small product intensities and the necessity of subtracting the background which results primarily from overlap of the Ar⁺ mass peak into the ArH⁺ mass peak (about 0.5% of the Ar⁺ peak intensity at the mass resolution used). The magnitude of the cross sections was checked at several energies by detailed measurements of the product intensities as a function of pressure (see Sec. III A). The cross sections determined from pressure-dependence studies according to Eq. (9) agree with the energy scan results within one standard deviation. The horizontal bars in Fig. 7 represent the estimated ±0.05 eV uncertainty in the laboratory energy. Similar uncertainties apply to all cross sections reported in this work.

The data for the D₂ reaction are compared to the H₂ results at the same center-of-mass energies in Fig. 8. Cross sections for the two processes are nearly identical, both in magnitude and the relative behavior as a function of energy. Differences are within one standard deviation at all but the highest energies. Above about 10 eV, the data for H₂ and D₂ exhibit somewhat different behavior. The cross sections are, however, within an experimental uncertainty of two standard deviations from one another. We cannot definitively conclude whether the apparent deviations are in fact significant.

The present results for the reaction cross section are compared to reliable previous determinations in Fig. 9. Since we find small or no differences in the total cross sections for H₂ and D₂, both reactions are plotted together.

FIG. 7. Cross section for reaction (1) as a function of the argon ion kinetic energy in the laboratory frame (upper scale) and the center-of-mass frame (lower scale). Each point represents an average of several determinations. The vertical error bars indicate ±2 standard deviations. The horizontal error bars indicate the uncertainty in the nominal ion energy (±0.05 eV lab). The dashed line gives the cross section predicted by the LGS model for ion–molecule reactions. The arrows indicate the critical energies, Table II, for product dissociation according the simple direct reaction models discussed in the text. From left to right, the arrows indicate E_S, E_R, E_S^*, and E_R^*.
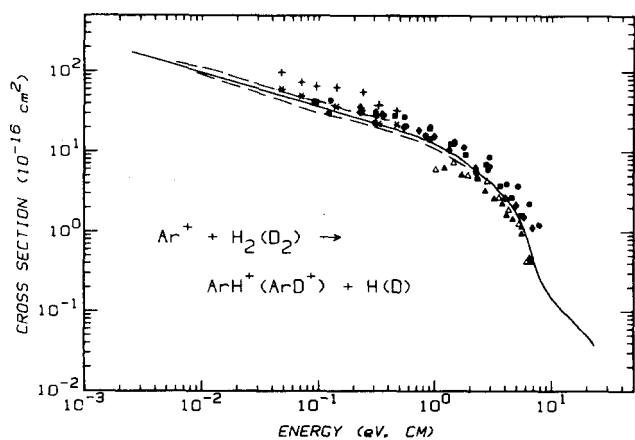
FIG. 9. Literature values for the cross sections of reactions (1) and (2) as a function of center-of-mass energy. The solid line represents the present data for reaction (1). Previous beam guide results of Teloy and Gerlich (Ref. 14) are given by the lower dashed line (D_2) and upper dashed line (H_2). Ion beam/gas cell results are given by solid symbols for D_2 and open symbols for H_2: ●, Henchman (Ref. 11); ◆, Hyatt (Ref. 15); ■, Homer (Ref. 16); ▲ and △, Henglein (Ref. 17). State-selected TESICO results (Ref. 29) are given for (^2P_J)Ar$^+$ + H_2: *, J = 3/2; +, J = 1/2.

Conventional ion beam/gas cell investigations of this reaction[11,13,15–17] are in general agreement with our results, although the scatter in the data of different laboratories illustrates the experimental uncertainties inherent in such experiments. It has been pointed out[75] that early work of Giese and Maier[18] (not shown) is in error due to inappropriate correction factors which were applied. Recently reported results of Klein[12] (not shown), for which experimental details have not been published, are too low by a factor of about 4. Previous guided beam results of Teloy and Gerlich[14] from 0.01 to 1.0 eV show excellent agreement in the relative behavior of $\sigma(E)$. Our results fall between their studies in magnitude.

Figure 9 also shows TESICO[29] results for the Ar$^+$(^2P_J) state-selected cross sections for reaction (1). The J = 1/2 state cross section is ∼1.5 times larger than for the J = 3/2 state. For reaction (2), the J = 3/2 cross section is essentially the same in magnitude as for reactions (1) and the cross section for J = 1/2 is enhanced by 1.3 times. The slope of the TESICO results agree closely with our results, but the absolute magnitudes are larger than ours for both spin-orbit states. The J = 3/2 results are just within the upper uncertainty limits of our results, which could be interpreted to mean that our ion beam contains primarily Ar$^+$($^2P_{3/2}$). It is more likely that our ions have a near statistical 2:1 population of J = 3/2 and J = 1/2, respectively. This suggests that the TESICO results are systematically high. In the TESICO experiments, 20% to 25% of the ions escaped detection due to collection losses and rather large correction factors were applied to account for collection losses and secondary reactions.

Four distinct regions can be discerned in the total reaction cross sections for reactions (1) and (2). At low energies, E < 0.8 eV, the total cross section for reactions (1) and (2) is proportional to $E^{-0.42\pm0.03}$, as determined by a least-squares fit to the data. The LGS model[41] of ion–molecule reactions, based on the long-range ion-

induced dipole potential, predicts an $E^{-0.5}$ behavior for the cross section and a slightly larger magnitude. The LGS prediction is shown in Fig. 7 for comparison with the data. The experimental cross section approaches within 10% of the LGS limit at 0.5 to 0.7 eV. At intermediate energies, $1 < E < 4$ eV, the cross section falls off with an $E^{-1.1\pm0.1}$ dependence. At a higher energy, $5 < E < 7$ eV, the cross section declines sharply as $E^{-4.2\pm0.2}$.

A previously unknown feature in the cross section is found at the highest accessible energies, $E > 7$ eV. Rather than continuing its sharp fall off, the cross section displays a "lump" at these energies. (A similar but much more prominent high-energy feature in the analogous reactions of Kr$^+$ has been reported by Klein[12] and confirmed by us.[76]) This behavior is suggestive of the onset of an endoergic reaction channel. An empirical deconvolution of the feature can be obtained by extrapolating the $E^{-4.2}$ region of the cross section to these higher energies and subtracting it out. The resulting curve has an apparent threshold of 8 ± 1 eV. The scatter in the data prevents a more precise determination of this "threshold" or a meaningful comparison between reactions (1) and (2).

B. Ar$^+$ + HD

The excitation functions of reactions (3a) and (3b) are presented in Fig. 10, along with their sum which is compared to reaction (1). The branching ratio for the two isotopic products is shown in Fig. 11. The near absence of an *inter*molecular isotope effect in the cross sections for the reaction with H_2 and D_2 contrasts sharply to the observed *intra*molecular isotope effect for the reaction with HD. The total HD cross section agrees well within experimental error with the H_2 and D_2 cross sections in the low and moderate energy regions, $E < 4$ eV. The $\sigma(ArH^+)/\sigma(ArD^+)$ ratio is close to unity throughout the low energy region, but decreases as the energy decreases. A reversal occurs at 0.14 eV, below which the deuteride
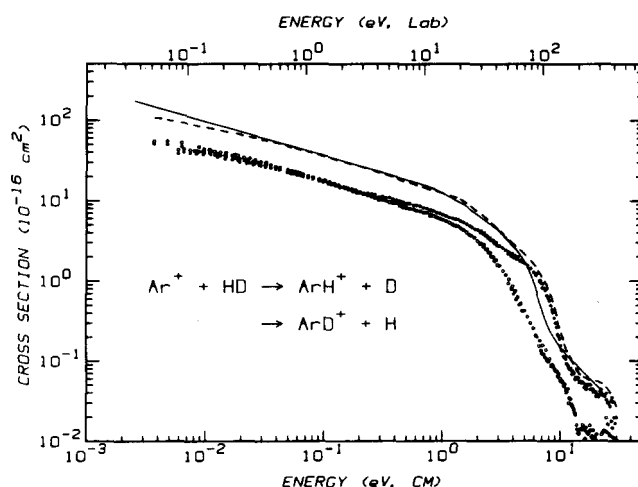

FIG. 10. Data for reactions (3a) and (3b) as a function of the argon ion kinetic energy in the laboratory frame (upper scale) and the center-of-mass frame (lower scale). The solid circles show the cross section for reaction (3a), formation of ArH$^+$, and the open circles show reaction (3b), formation of ArD$^+$. The dashed line indicates their sum. The solid line represents the data for reaction (1) for comparison. Relative uncertainties in the total cross sections are similar to those for reaction (1) in Fig. 7.
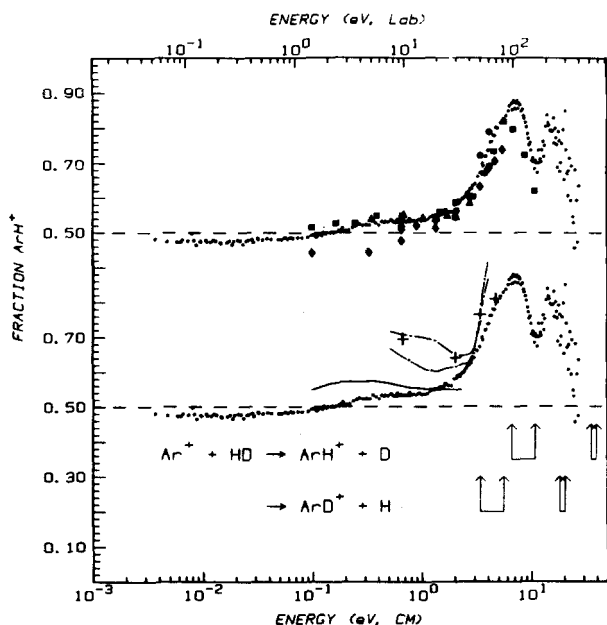
FIG. 11. Isotopic branching ratio for reaction (3) presented as the fraction of ArH^+ product. The ratio is plotted as a function of the argon ion kinetic energy in the laboratory frame (upper scale) and in the center-of-mass frame (lower scale). Two plots are shown for clarity and are offset on the vertical axis. The upper plot compares the present data (small points) with literature results for the isotope ratio: ●, Henglein (Ref. 17); ■, Klein (Ref. 12); ▲, Koski (Ref. 26); ◆, Futrell (Ref. 27). The lower plot compares the present data (small points) to several theoretical models: —— orientation isotope effect, Hierl (Ref. 32); +, classical kinematic model, Suplinskas (Ref. 50); - · - (case a) and - - - (case b), quantum mechanical multiple-collision calculation, Yuan (Ref. 52). The arrows indicate the critical energies, Table II, for product dissociation according to simple direct reaction models discussed in the text. The upper row of arrows is for ArH^+ products and the lower row is for ArD^+. From left to right, the arrows indicate E_S, E_R, E_S^*, and E_R^*.

product channel is favored. The ratio reaches a value of ~0.9 at the lowest accessible energies.

At higher energies, there are significant differences between the HD total cross section and the H_2 and D_2 cross sections. The sharp fall-off region shifts to higher energies for HD compared to either homonuclear system. Examining the ArH^+ and ArD^+ channels separately illuminates this effect. The ArD^+ channel starts a fall-off with an energy dependence of $E^{-2.5\pm0.3}$ from about 2.5 to 6 eV. Above 2.5 eV the reaction is dominated by ArH^+ production. The ArH^+ channel exhibits a moderate decline, $\sigma \propto E^{-1.1\pm0.1}$, from 2.5 to 7 eV, then falls off sharply as $E^{-6.0\pm0.3}$ above 7 eV.

At the highest energies corresponding to the lump feature of reactions (1) and (2), HD shows similar behavior. The ArD^+ cross section shows a slight inflection at about 8 eV, but then continues a sharp decline above 10 eV. The hydride ion has much larger lump and does not fall off until the upper bound of the experimental energy range (30 eV). This behavior is particularly evident in the nonmonotonic behavior of the isotope ratio, Fig. 11. Although the scatter is rather large at high energies as a consequence of the division of the small cross sections values, several regions are evident. The branching ratio first increases sharply at about 5 eV as the deuteride

begins its initial fall-off, then decreases as the hydride also falls off. A second increase and decrease in the ratio occurs at high energy corresponding to the lump feature in the cross section.

In Fig. 11, the present results for the isotope ratio are compared with earlier determinations by conventional ion beam methods.[12,17,26,27] The agreement is generally good within the uncertainty of the previous results over the range of overlap in energies. The results of Futrell[27] are an exception to the overall agreement—they show the deuteride product being favored well above the reversal at 0.14 eV. The nonmonotonic high energy feature is seen here for the first time. Earlier high pressure mass spectrometric studies by Klein and Friedman[28] (not shown) indicate the reversal of the intramolecular isotope effect at a mean energy of 0.2 eV, in general agreement with the present results. Because of the large energy distributions in those experiments, the ratios are not directly comparable to the present work.

C. Charge transfer channel

While the hydrogen atom transfer reactions (1) through (3) form the primary focus of this work, we have made limited measurements of the charge transfer channel, reaction (9). Several special experimental problems are involved in making measurements of reaction (9). Charge transfer products can be formed in a near-resonant process corresponding to a long-range electron jump in which little or no momentum is transferred to the products.[32] Complete collection of such products from the octopole requires the pulsed beam arrangement described earlier. However, measurement of the charge transfer channel for this system poses other experimental difficulties, described below, which make the pulsed beam arrangement of marginal utility. For this reason, we have performed only the normal continuous beam experiments on reaction (9) and therefore collection of the products from the octopole may be less than 100%.

Once the charge transfer products are extracted from the octopole trap and injected into the quadrupole mass filter, their forward energy may be very different than that of the primary ions. For the extreme case of no momentum transfer, the H_2^+ ions are essentially thermal and therefore have a laboratory energy which is lower than the primary ion energy by the full amount of the lab ion energy. Raising the quadrupole analysis energy for such ions can compensate for this effect. In the present case, however, that can be done only to a limited extent while still adequately resolving the hydrogen ions (mass 2) from the primary ions, which are transmitted through the quadrupole mass filter at "zero" mass.

Despite these difficulties it is possible to measure the charge transfer channel cross sections for laboratory energies below about 20 eV lab (2 eV c.m. for the D_2 system). The deuterium reaction was studied so that a lower quadrupole resolution could be tolerated. The results are shown in Fig. 12. Despite the experimental difficulties associated with this reaction, we have probably collected more than 50% of the products at the lower energies. At
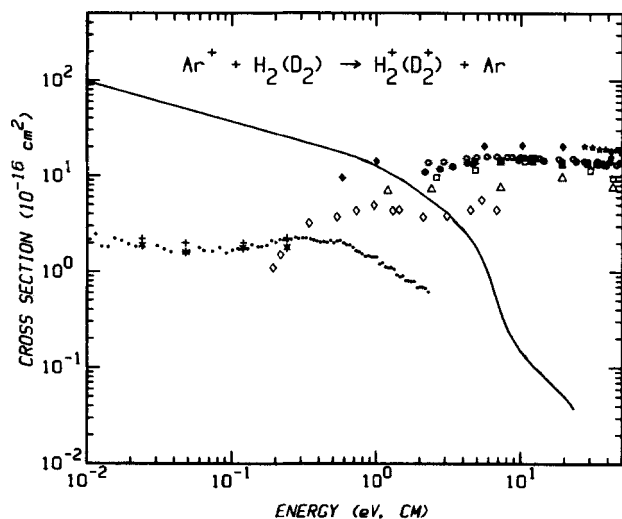
FIG. 12. Cross sections for the charge transfer reaction of Ar^+ with H_2 and D_2 as a function of the argon ion kinetic energy in the center-of-mass frame. The present results for the D_2 charge transfer reaction are given by the small points. State-selected TESICO results for $(^2P_J)Ar^+$ with D_2 are given by + $(J = 1/2)$ and $*$ $(J = 3/2)$. Results from conventional ion beam/gas cell experiments (with H_2 except as noted): ■, Ghosh (Ref. 38); O and ● (D_2), Amme (Ref. 36); ◆, Gilbody (Ref. 39); △, Gustaffson (Ref. 37); ★, Hedrick (Ref. 33); ☐, Wolf (Ref. 40); ◇, Mahadevan (Ref. 35). The solid line represents the data for reaction (1).

higher energies, discrimination against the slowest products may account for the decline in the apparent cross section. Figure 12 also compares the results to the deuterium atom transfer channel and to charge transfer results obtained by other researchers.[29,33,35–40] The only literature results at low energies are those of Tanaka et al.[29] The agreement with our results is rather remarkable (perhaps fortuitous) considering the differences in instrumentation. At relative energies greater than 10 eV, where most experimental determinations have been performed, the charge transfer cross sections are larger than those at lower energies. The only set of data which overlaps the two regions is that of Mahadevan,[35] who measured only slow ion production. The correspondence to the other results is poor at both ends.

D. Deconvolution

The Doppler broadening discussed above (Sec. III B) is a substantial effect below about 0.1 eV. While it is not possible to determine a unique form for the true cross section from the energy-broadened results, we can make some inferences about the true behavior.

The form of the convolution function for Doppler broadening [Eq. 14] is such that the LGS cross section, $\sigma_{LGS}(E) \propto E^{-m}$ with $m = 0.5$, is unchanged by the broadening effects. Convolution of power law cross sections with larger or smaller exponent m results in phenomenological cross sections which have slopes closer to the LGS cross section, but which exhibit significant negative or positive curvature, respectively. Thus, no cross section of the form E^{-m} when convoluted can reproduce the $E^{-0.42}$ dependence of the data. Rather, the true cross section must curve downward with decreasing energies,

or even exhibit a threshold at a very low energy. In Fig. 13, we have plotted two quite different forms for the cross sections which result in an adequate representation of the data after convolution. The first is a threshold model given by

$$\sigma(E) = \sigma_0 \cdot (E - E_T)^n/E, \tag{18}$$

where σ_0 is an energy-independent scaling factor and E_T is the threshold energy. This form with $n = 0.5$ can be derived using microscopic reversibility arguments for endoergic ion–molecule reactions.[77] It corresponds to an additional energy barrier E_T added to the centrifugal barrier for the charge-induced dipole potential, either in the entrance or exit channel. Reasonable fits to the present data (after convolution) are obtained with $n = 0.5$ and $E_T = 8 \pm 4$ meV. A significantly better least-squares fit to the data can be obtained by allowing the exponent n to vary. Figure 13 shows the best fit for this threshold function (curve A), with $\sigma_0 = 13.7$, $n = 0.56$, and $E_T = 4.7$ meV. The other model cross section shown in Fig. 13 (curve B) is a capture collision model cross section based on a frozen rotor approximation to the long range potential. This model is described in the Discussion section. While the convolution of A gives a slightly better least-squares fit to the data than the convolution of B, it is clear from Fig. 13 that the two are nearly indistinguishable. This result illustrates that the apparent cross sections are insensitive to the behavior of the true cross section below ~0.01 eV, as expected due to the Doppler broadening effect (Sec. III B). On the other hand, the true cross section must behave very similarly to both A and B above about 0.03 eV. While other functional forms for the cross
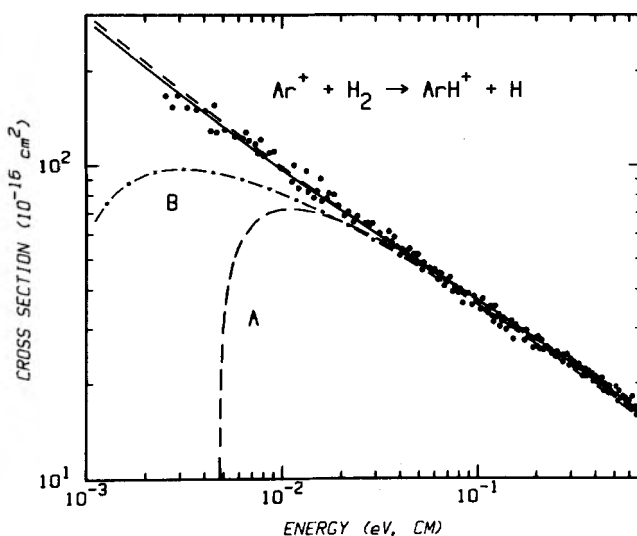

FIG. 13. Model cross sections compared with the data for reaction (1) at low energies. The points are the present data for reaction (1), the same as in Fig. 7. Curve A is the threshold model, $\sigma = \sigma_0(E - E_T)^n/E$ with $\sigma_0 = 13.7$, $E_T = 4.7$ meV, and $n = 0.56$. The solid line gives this form convoluted with the experimental energy distributions. Curve B gives the capture-collision cross section calculated with a frozen-rotor approximation to the long range charge-induced dipole and charge-quadrupole potentials (see the text). The rotor angle was fixed at 43.1°. The corresponding convoluted cross section is given by the short dashed line.

section may be consistent with the data, we can confidently exclude any cross section with a threshold greater than about 15 meV as well as pure power law cross sections, E^{-m}.

E. Reaction rates

Figure 14 presents the phenomenological rate constants as a function of kinetic energy for reaction (1). The data are the same as in Fig. 7, but have been converted to rates according to Eq. (16) and plotted vs the mean relative energy $\langle E \rangle$. The rates are compared to recent flow/drift tube results.[4,7] The agreement is excellent, both in magnitude and energy dependence, demonstrating that the present techniques can truly bridge the gap between thermal experiments and high-energy experiments.

Room temperature reaction rates are determined by direct conversion of the cross sections to phenomenological rates at the lowest ion energies. The rate constants are $k_1 = 9.5 \pm 2$, $k_2 = 8.0 \pm 3$, and $k_3 = 8.6 \pm 3$ ($\sim$53% ArD⁺; $\sim$47% ArH⁺) for reactions (1), (2), and (3), respectively, in units of 10^{-10} cm³ s⁻¹. The uncertainties for the rate constants include the uncertainties in the cross sections and in the energy as well as errors due to the extrapolation procedure. Reactions (2) and (3) have larger uncertainties since the data do not extend to energies as low in the center-of-mass frame. The intermolecular isotope effect on the rate constant due to mass factors alone predict ratios of $1.0 : 0.727 : 0.825$ for $k_1 : k_2 : k_3$. The apparent deviations from these ratios in the experimental rates are much smaller than the uncertainties and are probably not significant.

The translational temperature dependence of the thermal rate constant for reaction (1) from 100 to 50 000 K is presented in Fig. 15. The vibrational and rotational temperature of the H₂ is established by the gas cell

FIG. 15. Thermal rate constant for reaction (1) as a function of the translational temperature. The solid curves give the temperature dependence of the thermal reaction rate derived from the present data. At low temperatures, the curves are based on the threshold model cross section (lower solid curve) and the frozen-rotor capture model (upper solid curve). These correspond to curves A and B in Fig. 13, respectively. The broken lines give experimental upper and lower limits (see the text). The symbols give literature values from Table I: ×, Bowers (Ref. 3); ■, Dotan (Ref. 4) and Lindinger (Ref. 7); +, Rakshit (Ref. 5); ▲, Smith (Ref. 8); ▼, Ryan (Ref. 9); ●, Henchman (Ref. 11); ♦, Gaucherel (Ref. 6); vertical bars, Adams (Ref. 10).

temperature ($\sim$305 K). Above $T_k \approx 1000$ K, the data was integrated directly according to Eq. (17). At lower temperatures, assumptions about the true, unconvoluted behavior of the cross section must be made. The lower solid line is the rate obtained using the threshold model cross section (curve A in Fig. 13); the upper solid line is from the frozen-rotor capture model (curve B). A strict upper limit to the rate constant is obtained by extrapolating the observed low energy power law dependence of the phenomenological cross section, i.e., $\sigma(E) \propto E^{-0.42}$, to zero energy. This is shown by the upper broken line in Fig. 15. The lower dashed line is a conservative lower limit, determined using the threshold form of Eq. (14) with $n = 0.5$ and $E_T = 0.015$ eV, the highest threshold consistent with our data. The uncertainty in the absolute magnitude of the rate constant is the same as for the cross section, ±20%. Smoothing the data before integration and using independent data sets results in deviations of less than 5%. Because D₂ and HD total cross sections are nearly identical to the H₂ reaction cross section, the rate coefficients for these reactions have virtually the same temperature dependence as that shown in Fig. 15, but the magnitudes are smaller according to the mass factor in Eq. (17).

Rate constants obtained by other researchers are presented in Table I and also in Fig. 15. At 300 K, the most recent ICR[3,8] and flow/drift tube[4,7] results agree nicely with our rate determination. Single source mass spectrometric results[9,11] lie outside the range of other determinations. These are probably in error; accounting for secondary reactions and back reaction is difficult in
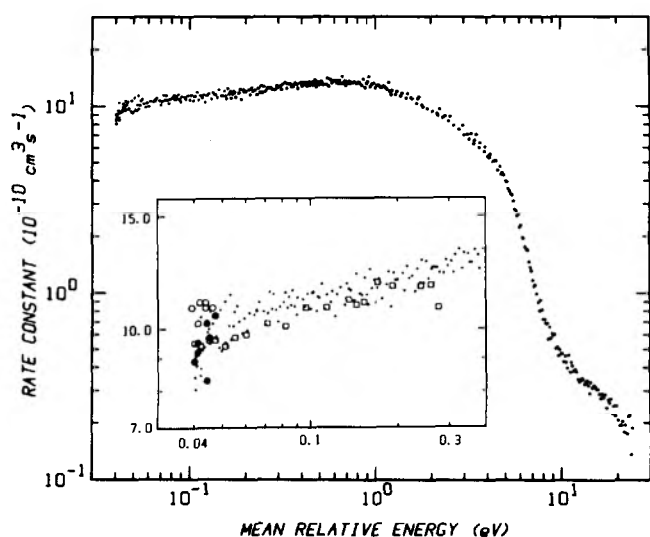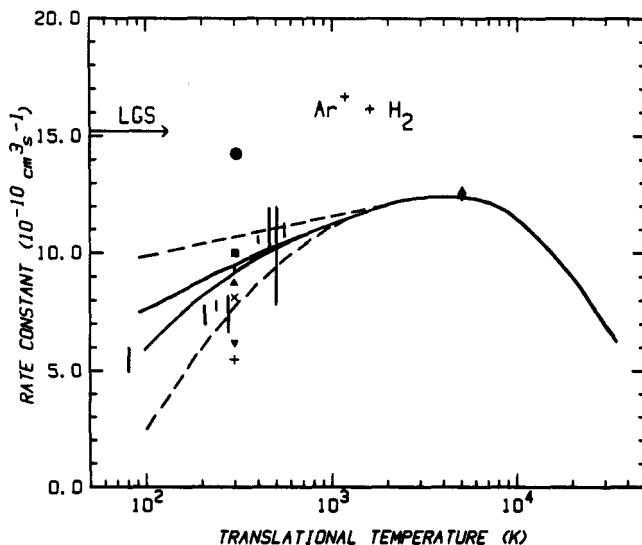

FIG. 14. Phenomenological rate constant for reaction (1) vs the mean relative energy of the reactants, $\langle E \rangle$. The small points show the present results, which are the same data as in Fig. 7 converted to the reaction rate as described in the text. The inset compares the present data to flow/drift tube results in an argon buffer gas, ●, Lindinger (Ref. 7) and ○, Dotan (Ref. 4); and in a helium buffer, □, Dotan (Ref. 4).

TABLE I. Thermal rate constants for the reaction $Ar^+ + H_2 \rightarrow$ products.

Technique[a]	Products	Rate constant[b]	Reference
GIB	ArH+	9.5 ± 2	this work
ICR	total	8.1 ± 2	3
FD	total	10 ± 2	4
DT	ArH+	5.4 ± 1.1[c]	5
FD	ArH+	10 ± 3.5	7
ICR	total	8.8 ± 0.5	8
MS	ArH+	6.2	9
MS	ArH+	14[d]	11
FAG	total	9	10
PJ	ArH+	12.5[e]	6
LGS model	total	15.2	

[a] GIB: guided ion beam; ICR: ion cyclotron resonance; FD: flow/drift tube; MS: single source mass spectrometer; DT: drift tube; FAG: flowing afterglow; PJ: plasma jet.
[b] 10^{-10} cm^3 s^{-1}; at ~300 K except as noted.
[c] $Ar^+(^2P_{3/2})$. See footnote 78.
[d] "Best" pre-1972 mass spectrometric value according to review by Henchman (Ref. 11).
[e] Translational temperature 5000 K.

such experiments. A drift tube result[5] is lower than all other results; however, the data interpretation has been disputed.[78] The temperature dependence of the rate from flowing afterglow experiments[10] agrees only roughly with our results. The discrepancies could arise from the different internal temperatures of the H_2 reactant. It has been noted,[11] however, that the flowing afterglow results were subject to systematic variations with pressure, which may indicate that secondary reactions influence the results. The only available rate at high temperatures is from a plasma jet study at T_k = 5000 K, in which the vibrational temperature was ~300 K.[6] It is in near perfect agreement with our result.

At low temperatures, the rate clearly increases with temperature. This indicates that at low temperatures there is a small activation energy, defined in the Arrhenius sense as $E_a = d(\ln k)/d(1/k_BT)$. At 300 K, the activation is between 2 meV (from the upper limit rate) and 15 meV (from the lower limit). The higher value is equivalent to the threshold in Eq. (18), as can be shown analytically for this form of the cross section with n = 0.5. The activation energies from the rates calculated from the "best fit" cross section models (solid lines in Fig. 15) are 6 ± 2 meV at 300 K. At translational temperatures greater than about 3000 K, the rate constant begins to decrease as the energies in the fall-off region of the excitation function (E > 1.0 eV) are accessed.

V. DISCUSSION

A. Low energy behavior

The very large reaction cross sections at low energies (<1 eV) indicate that the strong long-range attractive potential between the argon(1+) ion and the hydrogen molecule plays a major role in determining the overall reactivity. From early studies of these reactions, it was thought that the excitation functions at low energies were adequately described (both in magnitude and energy

dependence) by the LGS model, which gives the capture collision cross section for the ion-induced dipole potential.[41] The present experimental results clearly show deviations from the LGS model. The apparent cross sections range from two-thirds σ_{LGS} at thermal energies up to about 90% at ~0.6 eV (Fig. 7). Consideration of the effect of experimental energy broadening indicates that the deviation is actually more pronounced than is evident from the apparent cross sections (Fig. 13).

The LGS model involves two basic assumptions: (1) the collision cross section is determined by the ion-induced dipole long-range potential and (2) reaction occurs upon every orbiting collision. The first assumption is incorrect in this case since H_2 has a permanent quadrupole moment which alters the long range potential. The second assumption, which is really an upper limit, may be questionable in this case. As noted in the introduction, reactions (1) through (3) involve an avoided crossing between the Ar^+-H_2 and $Ar-H_2^+$ asymptotic surfaces to reach the ArH^+-H product region. The lower adiabatic surface can also lead to charge transfer as well as atom transfer, but the charge transfer cross section is much too small to account for the deviation of the atom transfer cross section from LGS. The avoided crossings between the Ar^+-H_2 and $Ar-H_2^+$ surfaces occur at Ar–H_2 separations in the vicinity of 4 to 5 Å.[47] The position of the centrifugal barrier which determines the orbiting collision cross section for long-range potential models is energy dependent; for the LGS model it lies beyond 5 Å region only for relative energies below 0.03 eV. A detailed understanding of the low energy behavior of reactions (1) through (3) thus requires consideration of both the long-range potential which brings the reactants together and the short-range interactions which determine the probability of transition to the reactive potential energy surface.

1. Long range potential

The charge-quadrupole potential has a $1/r^3$ dependence—stronger than the $1/r^4$ dependence of the charge-induced dipole potential—and is either attractive or repulsive depending on orientation. The full long-range potential energy is given by

$$V(r, \theta) = -q^2\alpha/2r^4 + (3 \cdot \cos^2 \theta - 1)$$
$$\times [-q^2(\alpha_{||} - \alpha_\perp)/6r^4 + Qq/2r^3], \qquad (19)$$

where r is the intermolecular separation, θ is the angle between the H_2 axis and the line of centers, q is the ion charge, $\alpha_{||}$ = 0.934 × 10^{-24} cm^3 and $\alpha_\perp$ = 0.718 × 10^{-24} cm^3 are the parallel and perpendicular components of the polarizability of H_2,[79] $\alpha = (\alpha_{||} + 2 \cdot \alpha_\perp)/3$ is the spherically averaged polarizability, and Q = +1.23 × 10^{-26} esu cm^2 is the H_2 quadrupole moment.[80] The charge-quadrupole potential is repulsive for θ = 0° (collinear) and attractive for θ = 90°. The anisotropic polarizability, in contrast, produces a stronger ion-induced dipole attraction in the collinear orientation than in the perpendicular. However, the anisotropy of the polarizability is a relatively minor effect.

The anisotropy of the potential represented by Eq. (19) makes an exact calculation of the capture collision cross section difficult. A first order approximation can be obtained by holding θ constant in Eq. (19), then calculating the cross section on the resultant orientation-independent $V(r)$ according to the Langevin criterion for overcoming the centrifugal barrier. Cross sections calculated for this frozen rotor approximation are plotted for several angles in Fig. 16. For $\theta = 90°$, the charge-quadrupole potential is most attractive and the cross section is much larger than the LGS model. This corresponds to the locked quadrupole model of Su and Bowers,[81] except that we also include the anisotropy of the polarizability. The frozen rotor cross section is equivalent to LGS for $\theta = \cos^{-1}(1/\sqrt{3}) = 54.7°$. For smaller angles, the repulsive part of the potential causes the cross sections to decrease at very low energies or exhibit a threshold. We find that the simple frozen rotor model reproduces the energy dependence of the cross section (after convolution) with $\theta = 43.1°$. This form is plotted in Fig. 16 and also in Fig. 13 (curve B), where its convoluted form is compared with the data. The frozen rotor model (with θ as the only adjustable parameter) reproduces the data quite well, although slightly less well than the empirical threshold model (with three adjustable parameters: σ_0, n, and E_T). This result may be viewed as an indication of the average angle, and thus the average long range potential, for reaction between Ar^+ and H_2.

Physically more realistic models should include an average over all initial angles, the effect of H_2 rotational energy, and reorientation effects induced by the anisotropic potential. The second and third effects may be considered negligible at higher energies, $E \gg k_B T$, where the collision

time is much smaller that the H_2 rotational period[.] By averaging the frozen rotor cross sections over an isotropic distribution of angles, we obtain an averaged cross section that is slightly larger than σ_{LGS}, corresponding to a mean angle of approximately $60°$. This contrasts with the empirically obtained "average angle" of $43.1°$.

At low energies it is necessary to take into account the rotational motion of the H_2 and reorientation effects. Two general methods have been proposed which do this by averaging the angular part of $V(r, \theta)$, then applying the Langevin capture criterion to the averaged $V(r)$. In the average quadrupole orientation (AQO) model of Su and Bowers[81] an average orientation angle is calculated as a function of r by explicitly considering the rotational energy. Celli, Weddle, and Ridge[82] use a thermodynamic approach which averages $V(r, \theta)$ at each r for a statistical ensemble of orientations. While these models make some severe assumptions,[83] they currently provide the most reasonable estimates to the true capture-collision cross section for anisotropic potentials $V(r, \theta)$. Both these orientation-averaged potential models give capture cross sections higher than the LGS model at all energies for the $Ar^+ + H_2$ system. The experiments show the opposite effect; therefore, these models do not account for the results.

In the frozen rotor approach, a single angle—independent of both energy and the distance at which the centrifugal barrier occurs—was found to adequately represent the experimental results. This suggests a modification of the orientation-averaged potential models which would include a reaction probability with an orientational dependence. In order to reproduce the experimental results, this reaction probability would have to weight collinear orientations (which are repulsive at long range) more heavily than the perpendicular (attractive) orientations. To explore this idea further, we next consider the short range chemical forces which influence the reaction.

2. Short range interactions

Short range forces could provide an explanation for a preference for collinear and near-collinear reactions. The DIMZO calculations[47] indicate that the collinear surface is quite attractive, has a slightly deeper well than other geometries, and has a smaller barrier in the product channel than other geometries. Also, the collinear collision geometry could enhance the surface hopping probability. Calculations[46,48] indicate this nonadiabatic behavior is aided by vibrational motion of the H_2 molecule. In collinear collisions, the relative translational motion can couple with the vibrational motion more efficiently than in perpendicular collisions.

Instead of a reaction model which includes an orientational dependence, the results can also be explained by the presence of a mean activation barrier. The experiments indicate there is an activation energy in the Arrhenius sense of roughly 6 meV. The DIMZO surfaces[47] indicate no barrier in the potential energy surfaces, but according to the trajectory calculations[46] and the calculated
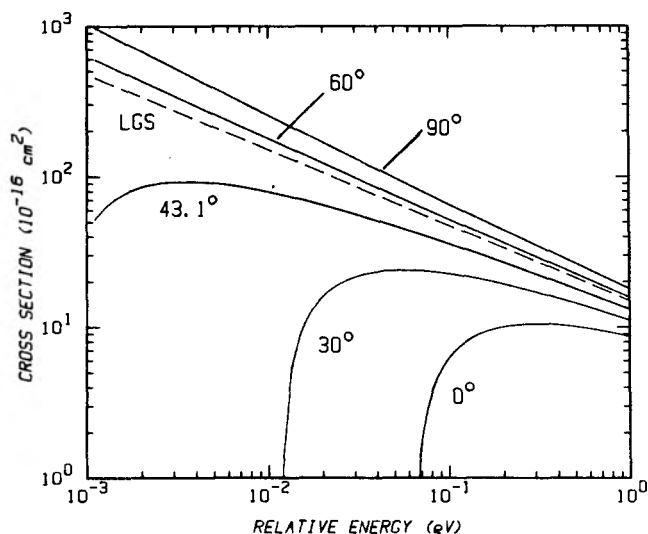

FIG. 16. Capture collision cross sections according to the frozen rotor approximation on the long range charge-quadrupole and charge-induced dipole intermolecular potential for $Ar^+ + H_2$ as a function of the relative energy of reactants. The frozen rotor cross sections are given for several fixed angles: $\theta = 0°$ (collinear) is the most repulsive and $\theta = 90°$ (perpendicular) is the most attractive. The curve for $\theta = 43.1°$ represents the best fit of the present data for reaction (1) after convolution with the experimental energy distributions (see also Fig. 13). The dashed line gives the LGS cross section, which also corresponds to the frozen rotor model with $\theta = 54.7°$.

nonadiabatic transitions probabilities[48] there are constrictions at the crossing between the two entrance valley potential energy surfaces. For collinear reactions, a translational threshold of $\sim$0.06 eV for nonadiabatic transitions was obtained by Baer.[48] While the present results are consistent neither with such a large energy barrier nor with a large increase in the reaction probability at 0.06 eV, it is not surprising that the one-dimensional model does not correspond quantitatively to experimental results. Baer's calculations imply that the magnitude of the predicted threshold is controlled to a large extent by the energy defect between the Ar^+–$H_2(v = 0)$ and Ar–$H_2^+(v = 2)$ surfaces. This would indicate that the transition probability should be quite different for the H_2, D_2, and HD reactions, which have different vibrational level spacings, and for the $J = 3/2$ and $J = 1/2$ spin-orbit states of Ar^+, which have different asymptotic energy levels. The present results, in contrast, show essentially no differences in the total cross sections for reaction with H_2, D_2, and HD. In addition, the TESICO results[29] indicate that there is no large enhancement for reaction (1) as a result of the near resonance between the $Ar^+(^2P_{1/2})$–$H_2(v = 0)$ and Ar–$H_2^+(v = 2)$ reactant states.

This apparent disagreement between experiment and the calculated nonadiabatic transition probabilities may arise from several factors. First, at low energies reaction may occur adiabatically on the lowest surface, which has $Ar^+ + H_2$ character for shorter H–H distances. The electronic surfaces are the same for all three isotopic hydrogen reactants, although the vibrational and rotational spacings differ. Second, noncollinear and nonzero impact parameter approaches of the reactants could exhibit lower barriers than given by Baer's collinear model. Third, the H_2 rotational motion could couple with the vibrational and translational motion to induce nonadiabatic transitions between the surfaces. Such coupling might be promoted by the anisotropy of the potential energy surfaces (both the long-range quadrupole anisotropy and short-range anisotropy evident in the DIMZO surfaces). We note that when all vibrational and rotational levels are considered, there are near resonances (within 0.02 eV) between the asymptotic Ar^+–H_2 and Ar–H_2^+ surfaces for each of the isotopic variants of hydrogen, reactions (1), (2), and (3), and for both spin-orbit states of Ar^+. Transitions between some of these states do require, however, substantial energy flow out of translation and into vibration and/or rotation of the H_2.

As pointed out by Chapman and Preston,[46] reaction can involve both adiabatic and nonadiabatic behavior in the region of strong interaction between the two entrance channel surfaces. The lower adiabatic surface is quite reactive, but some trajectories of the reactants will end up on the repulsive upper surface and return to the entrance valley, either as reactants or charge transfer products. The overall behavior of the reaction cross section at low energies would appear to be a consequence of both the long-range anisotropic potential and the short-range interaction between the potential energy surfaces.

3. Intramolecular isotope effect

The intramolecular isotope effect at low and moderate energies has been treated by Hierl in an orientation model for the rare gas ion/HD reactions.[53] Its basic assumption is that the atom transferred is the one that is directed towards the ion at the moment of the crossing of the centrifugal barrier or upon the crossing to the Ar–H_2^+ charge state surface, whichever occurs first. The orientation probability is calculated considering (1) the torque exerted on HD by the incoming ion due to the displacement of the center-of-mass from the center-of-polarizability of HD and (2) the HD rotational energy. The isotope ratio predicted by this model is shown in Fig. 11 for comparison with the data. Hierl's model successfully predicts the near 50% branching ratio for reaction (3) at low energies and the much larger preference for the hydride product in the reaction $Kr^+ + HD$. The agreement with the present results is reasonable considering the simplifying assumptions of the model. In particular, the model incorporates Gislason's prediction for the crossing between the two charge-state surfaces,[84] which has been shown to be a poor approximation by both Baer's and Tanaka's calculations.[46,48] Also, the anisotropic terms in Eq. (19) were not taken into account. The orientation isotope effect model was not extended to very low energies since the HD molecule could have time to reorient after crossing the centrifugal barrier or crossing to the other charge state surface. Thus, the model does not provide a quantitative explanation for the reversal of the isotope effect at 0.17 eV. It does, however, suggest that the deuteride product should be favored at very low energies: when the HD rotational energy is greater than the collision energy, it undergoes hindered, but full rotation in which the D atom is directed toward the argon ion most of the time. Thus, if the assumption that the reaction proceeds with the atom first encountered holds, the deuteride product should be favored.

Phase space considerations provide an alternate explanation for the deuteride being favored at very low energies. If the products are statistically distributed in the available phase space, the deuteride product is favored slightly. This is because the ArD^+ rotational/vibrational levels are more closely spaced than those of ArH^+ and the zero-point difference makes formation of ArD^+ slightly more exoergic. These effects are counteracted somewhat by angular momentum conservation constraints. A simple treatment[85] predicts $\sigma(ArH^+)/\sigma(ArD^+) \approx 1/\sqrt{2}$ or 0.71. The experimental ratio decreases to 0.9 at the lowest energies.

Statistical treatments are certainly appropriate if the reaction proceeds by a "long-lived" complex at low energies. Differential reactive scattering studies indicate, however, that the reaction is direct down to the lowest energy studied (0.1 eV).[19–23] It is conceivable that complex formation becomes important at the lower ion energies studied here, but this is not supported by the DIMZO surfaces, which indicate at most a shallow well corresponding to ArH_2^+. However, the statistical argument is

applicable without invoking a long-lived complex mechanism as long as there are strong interactions among all three atoms. It is not evident from the present experiments whether an orientational mechanism or a statistical process is responsible for the low-energy isotope effect.

B. Intermediate energies

At about 1 eV, the excitation functions for reactions (1) through (3) begin a mild decline, approximately as E^{-1}. This behavior clearly deviates from the capture-collision cross section due to the long-range potential. This deviation is not surprising since, as noted by Henchman,[11] the capture-collision model is not valid at higher energies because the centrifugal barrier merges with the repulsive core of the potential energy surface. At these energies, the collision cross section is more correctly estimated by the hard-sphere cross section—about 10 Å² for Ar⁺ + H₂. The results show, however, that the reaction cross sections also fall well below the hard sphere cross section above 1 eV. This cannot be attributed to product dissociation because the lowest-energy decomposition process,

$$\text{Ar}^+ + \text{H}_2 \rightarrow \text{Ar} + \text{H}^+ + \text{H}, \quad \Delta H_0^\circ = 2.3 \text{ eV} \quad (20)$$

is not energetically possible until higher energies. Rather, the decline in the cross section may be due to the onset of more diabatic behavior, in which some approaches of the reactants cannot reach the reactive Ar–H₂⁺ surface. This view is supported by the TSH study at 3.36 eV, which indicated that only about a third of the trajectories could lead to reaction.[46] The remaining reactants return instead to the entrance valley, resulting in either nonreactive scattering or charge transfer, reaction (9).

The reaction cross section falls off very sharply at energies above about 4 eV. This can be attributed to processes in which the nascent diatomic product has too much internal energy and subsequently dissociates. The reaction cross sections show no sharp break at the 2.3 eV threshold for reaction (20), indicating that the dissociative charge transfer is relatively improbable near the threshold. This is a consequence of the available energy being tied up in translation of the products.

Simple direct reaction models have been proposed to account for the velocity distributions of the products. Since energy conservation requires that the excess available energy go either into internal energy of the products or into product translational energy, such models can predict whether the diatomic product is formed in a stable state. The familiar spectator stripping model[24] assumes that the ion interacts only with one hydrogen atom, while the other "spectator" atom undergoes no change in velocity. Linear momentum conservation then fixes the translational energy of the products. The excess energy provided by the reaction exothermicity ends up as internal energy in the diatomic product. Above a certain reactant energy, the internal energy of the putative diatom exceeds its bond dissociation energy. This critical energy is given by[24]

$$E_S = (D_0^\circ + \Delta H_0^\circ) \cdot \left(\frac{m_A + m_B}{m_B}\right) \cdot \left(\frac{m_B + m_C}{m_A + m_B + m_C}\right) \quad (21)$$

in the center-of-mass frame, where B is the transferred atom and D_0° is the bond dissociation energy $D_0^\circ(\text{Ar–H}^+)$.[1] An obvious modification of spectator stripping is to allow some of the available energy to go into product translation. In a simple recoil model, all of the exothermicity ends up as translational energy of the separating products. This stabilizes the diatomic product and results in a critical energy of

$$E_R = (D_0^\circ) \cdot \left(\frac{m_A + m_B}{m_B}\right) \cdot \left(\frac{m_B + m_C}{m_A + m_B + m_C}\right) \quad (22)$$

which is substantially larger than E_S since ΔH_0° is negative for exothermic reactions.

These direct reaction models assume that the diatomic product dissociates whenever it has an internal energy greater than D_0°. High rotational excitation of the ArH⁺ product, however, could stabilize it above the zero-point dissociation energy. Production of rotationally quasibound states has been suggested by Farrar[86] for the formation of ArH⁺ from H₂⁺ + Ar. Such rotational excitation may occur if energy is released from bent configurations in the strong interaction region of the potential energy surface. Using the SCFMO[47] ground state potential curve of ArH⁺, we calculate that the highest possible rotationally bound state ($v = 0, J \approx 80$) is about 1 eV above D_0°.[87] This maximum value decreases rapidly with increasing vibrational excitation. While rotational stabilization would shade the critical dissociation points according to the stripping and recoil models to higher energies, the general features of the models are not affected.

E_S and E_R are listed in Table II for reactions (1) through (3) and are indicated by arrows in Figs. 7, 8, and 11. For all four isotopic variations of reaction (1), there is significant reaction above the spectator stripping limit. This alone indicates that the spectator stripping model is not fully applicable. Rather, the cross sections *begin* their sharp decline at about E_S. The decline continues up to the limit specified by the product recoil model, E_R. This suggests that the products are formed with a distribution of the available energy into translation or internal excitation, all the way from the spectator stripping extreme to the recoil model extreme. In the reaction with HD, the critical energies for deuterium atom transfer are lower

TABLE II. Critical energies for product dissociation.[a,b]

Reaction	E_S	E_R	$E_S^{\ddagger}$	$E_R^{\ddagger}$
(1)	4.60	7.52	24.5	27.4
(2)	4.50	7.36	24.0	26.8
(3a)	6.74	11.0	35.9	40.2
(3a)	3.45	5.65	18.4	20.6

[a] All energies in eV, center-of-mass frame.
[b] E_S spectator stripping model; E_R, recoil model; asterick indicates excited hydrogen atom production ($n = 2$).

than for hydrogen atom transfer. The heavier deuterium spectator atom carries away more translational energy for a given velocity, thus stabilizing the hydride product up to higher energies. This accounts for the sharp rise in the intramolecular isotope effect starting at E_S for reaction (3b), Fig. 11. Above the critical energies for reaction (3a), the isotopic branching ratio decreases again as the hydride products also undergo decomposition.

There are several mechanisms which allow the products to be produced with translational energies in excess of that predicted by spectator stripping. The DIMZO potential energy surfaces indicate that the product exit valley is somewhat repulsive.[47] The barrier in the exit channel is angle dependent, being 0.1 eV at 0° and ~0.5 eV at 90°. This repulsion would promote the recoil of the nascent products, but is probably not large enough to explain the large translational energy of the products in the recoil model limit. A classical kinematic model by George and Suplinskas[50] treats the reaction as a sequence of impulsive hard-sphere collisions among the three atoms. These collisions can result in products with excess translational energy. The prediction of this model for the isotope ratio is shown in Fig. 11. Also shown is the isotope ratio from the quantum mechanical multiple-collision calculation of Yuan and Micha.[52] While both of these models roughly predict the energy where the isotope branching ratio turns sharply in favor of the hydride (essentially at the spectator stripping critical energy), neither adequately reproduces the isotope ratio at lower energies. Further refinements of impulsive collision models may be able to explain the isotopic effect at these intermediate energies, but any comprehensive treatment must also provide for a smooth transition into the low energy region where orientational effects or statistical behavior are important.

C. High energy feature

The high-energy "lump" in the total cross sections is reminiscent of the onset of a reaction channel with an energy barrier. This inference is based on the expectation that the cross sections should fall off monotonically as the energy is increased. The cross section for atom capture should become smaller at higher energies as the repulsive core of the potential energy surface is sampled.[86] Also, based on the above discussion of direct reactions, we would expect the diatomic product to gain far too much internal energy to remain stable at such high collision energies. In order to account for the high energy reaction, it is necessary to find a repository for the excess available energy at collision energies above the apparent threshold of 8 ± 1 eV.

We first consider the possibility of high translational excitation of the products. In multiple impulsive collisions of the three atoms, the available energy can be converted into product translational energy. The sequential impulse model of Winn, Mahan, and Ruska[51] treats double collision processes of this type as well as single collision stripping-like collisions. This model has been used to explain differential scattering cross sections of exothermic ion–molecule reactions[88] and has also been extended to

integral cross sections of endothermic reactions.[89] We have calculated the sequential impulse model integral cross sections for reactions (1) through (3). The cross section for two-collision processes does result in stable products at energies well above 10 eV, but the cross sections have a very slow decline extending to high energy rather than the second sharp, delayed decline exhibited by the data. Also, the predicted intramolecular isotope ratio for reaction (3) is close to unity, in conflict with the experimental results. Recent modifications of the sequential impulse model by Safron[90] are unlikely to alter this basic behavior. Thus, while we cannot categorically rule out an impulsive mechanism for the high energy feature, these simple models are not consistent with the results.

The alternative to high product translational energies is electronic excitation of the products. One possibility is that the channel corresponds to the production of a stable or metastable excited state of ArH$^+$. For such a product to be detected, it must have a lifetime exceeding the 10 to 20 μs flight time between the interaction region and the detector or it must radiatively relax to the ground state. SCFMO calculations on the ArH$^+$ electronic states show no bound excited states up to about 10 eV above ground state ArH$^+$.[47] Approximate ab initio calculations[91] indicate that bound Rydberg states corresponding to Ar$(3p^5 4s^1)$ + H$^+$ and higher dissociation limits have energies starting at about 15 eV. These excitation energies are too large for production of such Rydberg states to correspond with the observed apparent threshold. Therefore, ArH$^+$ electronic excitation can be ruled out.

The other possibility for internal excitation is in the hydrogen atom product. The $n = 2$ electronically excited state lies 10.2 eV above the ground state. The threshold for formation of electronically excited hydrogen atoms, reaction (21),

$$Ar^+ + H_2 \rightarrow ArH^+ + H^*(n = 2) \qquad (23)$$
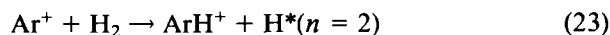
is 8.7 eV, close to the apparent threshold of 8 ± 1 eV of the high energy process. In reaction of helium ions with H$_2$, chemiluminescence from excited hydrogen atom products ($n = 2, 3, \cdots$) has been observed and the threshold for chemiluminescence agrees with the threshold for production of HeH$^+$.[92] It seems plausible that the analogous processes occur for the argon reaction. If we assume that reaction (23) is responsible for the high energy feature, we can apply the spectator stripping and product recoil criteria for diatomic product stability.[93] This simply involves adding 10.2 eV to the energy factors in Eqs. (21) and (22). These energies, denoted by E_S^* and E_R^*, respectively, are listed in Table II and indicated by arrows in Figs. 7, 8, and 11. The cross sections do show declines near these critical energies. In particular, the lower energy decline of the high energy feature observed for reaction (3b) as compared to reaction (3a) can be attributed to the lower critical energy for deuteride product. These results provide circumstantial evidence for excited hydrogen atom production. The higher excited states of hydrogen atom might also be expected, but with substantially smaller cross sections. If process (23) is occurring, it should be evident in differential reactive scattering

experiments (since the product velocities would be widely separated from those of ground state products) as well as in chemiluminescence studies. Unfortunately, no such experiments have been reported at these interaction energies.

Production of electronically excited products involves interaction on excited surfaces of the ArH_2^+ system. These are presumably accessed at high energies via crossings high on the repulsive core of the lower energy surfaces. However, very little is known about the details of the upper surfaces.

D. Competing processes

Up to now we have considered primarily the hydrogen atom transfer channel in $Ar^+ + H_2$ reactions. Charge transfer, reaction (9), and nonreactive elastic or inelastic scattering also occur and may be viewed as competing processes.

1. Charge transfer

In a crossed beam study of charge transfer, Hierl found that two mechanisms were operative.[32] The first is a long-range electron jump in which the H_2^+ product essentially retains the prior thermal velocity distribution of H_2 and is formed in the vibrational states most nearly resonant with Ar^+. The second mechanism involves intimate collisions of the reactants and results in large-angle scattering of the H_2^+ products and a large distribution of product vibrational states. This intimate collision mechanism is of little importance at the higher energy studied (3.44 eV), but is comparable in magnitude to the electron jump mechanism at the lower energies, 0.13 and 0.48 eV.

Before attempting a discussion of the experimental charge-transfer data, we caution that the present techniques and the TESICO experiments[29] may not detect slow products with 100% efficiency. For the high energy literature results,[33–40] the opposite is true, as the experiments are optimized for collection of slow products. Nevertheless, it is intriguing that the charge transfer channel is small relative to atom transfer at low energies, but relatively large at high energies where the atom transfer cross section is small. This suggests that the two processes compete with one another. Charge transfer is most likely at the high energies, where the electron-jump mechanism is preferred. This agrees with adiabatic models of charge transfer, which hold that charge transfer is most probable for near-resonant energy levels and at (high) collision energies where the collision time is comparable to the period of the electronic transition.[94] At low energies, this electron jump mechanism is not as probable and charge transfer may occur to a small degree via intimate collisions. As discussed previously, the strong interactions between the two entrance channel surfaces corresponding to Ar^+–H_2 and Ar–H_2^+ charge states can lead to the reactants being returned to the entrance valley region in the opposite charge state. Atom transfer is more probable, however, since the lower adiabatic surface is very attractive once it has been reached.

2. Nonreactive scattering

Intense nonreactive scattering was observed by Mahan and co-workers in differential cross section measurements on reaction (2).[19] They observed that the nonreactive scattering of argon ions on D_2 was very similar to the scattering on helium and was largely elastic. The nonreactive scattering cross section is larger than the atom transfer cross section in the range of 2.7 to 12.1 eV, although no absolute cross sections were given.[19] Moran and Cosby[95] measured scattering of Ar^+ on D_2 in the range of 1 to 1.5 eV. They reported that the total inelastic scattering cross section is on the order of 0.5×10^{-16} cm², while elastic scattering is at least ten times more probable. These results indicate that nonreactive scattering effectively competes with both atom transfer and charge transfer, at least at moderate and high energies. While it is possible to form ArH^+ products at high energies, charge transfer and nonreactive scattering processes are much more likely.

VI. SUMMARY

Guided ion beam techniques provide a versatile and accurate means to examine the translational energy dependence of ion–molecule reactions. The present work demonstrates that these techniques can span a range from thermal energies to very high energies in a single experiment. Comparison of the results to other methods for studying ion–molecule reactions, both in the thermal regime and at high energies, show generally excellent agreement. The 4π collection characteristics of the octopole beam guide means, of course, that information about the microscopic dynamics, i.e., the angle and energy of scattered products, is not accessible in these experiments. The reactant energy resolution, energy range, and sensitivity of the technique, however, allow a good deal of dynamical information to be inferred from the total reaction cross sections. In the following, we briefly summarize our observations on the argon ion–hydrogen reactions.

(1) The low energy cross sections are significantly smaller than those given by the Langevin–Giousmousis–Stevenson model for capture collisions due to the long-range ion-induced dipole potential. The quadrupole moment of H_2 is expected to make significant contributions to the capture collision cross section. Present models for approximating the capture rate on the anisotropic charge-quadrupole potential give cross sections larger than LGS, in conflict with the experimental result. A reaction probability which favors collinear and near-collinear reactions on the charge-quadrupole surface could produce this behavior.

(2) The total reaction cross sections for atom transfer from H_2, D_2, and HD are essentially identical at low energies, both in magnitude and energy dependence, when compared at the same relative energy. This indicates that the vibrational spacings and levels of the reactants are not critically important in determining the reactivity. While vibrational motion of the diatomic reactant is

expected to aid in transitions between the two diabatic electronic potential energy surfaces in the entrance channel, these results suggest that coupling with rotational or translational motion may also play a role.

(3) The intramolecular isotope ratio for reaction with HD is near unity at low energies. The deuteride product is slightly favored below ~ 0.14 eV c.m. It is not clear whether orientational or statistical effects are more important in producing this isotope effect.

(4) At about 1 eV, the cross sections begin to fall lower than the collision cross section. This could be due to increasing diabatic behavior in which many approaches of the reactants do not reach the reactive potential energy surface. Literature results show that charge transfer and nonreactive scattering dominate the Ar^+–H_2 interactions at higher energies. Our limited measurements of the charge transfer channel at low energies show that charge transfer accounts for only 2% to 10% of the total reaction below 1 eV.

(5) The reaction cross sections are dominated by effects due to the decomposition of the diatomic products above about 4 eV. Decomposition effects produce sharp declines in the cross sections and large intramolecular isotope effects. Comparison of the fall-off regions of the cross sections with the critical energies for product dissociation predicted by simple direct reaction models indicate that the available energy is broadly distributed between product translation and product internal excitation.

(6) A new feature in the reaction cross sections at high energies has been observed here for the first time. This feature probably represents the onset of an endoergic reaction channel. The energy dependence and isotope effects in this region are most easily explained by production of electronically excited hydrogen atoms. Since no direct evidence for this is observed in these experiments, however, other mechanisms cannot be ruled out.

APPENDIX: MULTIPOLE ION TRAPS

In this Appendix, the derivation of the effective trapping potential energy for a multipole ion trap is outlined and the effect of nonhyperbolic geometry of the multipole rods is considered.

Landau and Lifshitz[64] have treated the motion of a particle which is subject to a static field given by potential U_s and a rapidly oscillating force $F = F_0 \cdot \cos(\omega t)$, where F_0 is a function of the coordinates only. If the frequency of the oscillating part is large, a heavy particle will not be able to respond to the force during the period of an oscillation. This requirement is given by $\omega \gg 1/T$, where T is period of the motion which the particle would make in the potential U_s alone. Under these conditions, the motion of the particle can be described by motion in an effective potential[64]

$$U_{\text{eff}} = \frac{|F_0|^2}{4m\omega^2} + U_s. \tag{A1}$$

On top of the smooth trajectory due to this effective potential, there will be small, high frequency oscillations which average out over time.[14]

In the present context, U_s is simply the constant dc potential of the beam guide which determines the axial ion energy. The oscillating potential has only radial (r) and angular (θ) components and does not affect the axial (z) motion. The potential field of a multipole with rods of circular, rather than hyperbolic cross section cannot be represented exactly, but can be approximated as an expansion of hyperbolic multipole terms.[96] Thus, the electric potential is given by

$$\Phi = V_0 \cdot \sum_n a_n \cdot \left(\frac{r}{r_0}\right)^n \cdot \cos(n\theta), \tag{A2}$$

where each term corresponds to a $2n$-pole with weighting a_n, r_0 is the inner radius of the poles, and the rf voltage applied to adjacent rods is $+V_0 \cos(\omega t)$ and $-V_0 \cos(\omega t)$. An ideal octopole is given by one term with $n = 4$. Due to the octagonal symmetry, only terms in the potential which change sign upon a $\pi/4$ rotation are allowed. This limits the terms to $n = 4, 12, 20$, etc. Physical defects in the construction or alignment of the octopole rods could introduce other multipole terms.

The oscillating force on an ion inside the multipole trap is given by

$$F_0 = -q \cdot \nabla \Phi. \tag{A3}$$

Substitution of Eqs. (A3) and (A2) into Eq. (A1) gives the following result for the effective potential energy

$$U_{\text{eff}}(r, \theta) = U_s + \frac{q^2 V_0^2}{4m\omega^2 r_0^2} \cdot \sum_i \sum_j \left[ij a_i a_j \right.$$
$$\left. \times \left(\frac{r}{r_0}\right)^{i+j-2} \cdot \cos(i\theta - j\theta) \right]. \tag{A4}$$

The terms have been consolidated making use of the identity $\cos(\alpha - \beta) = \cos \alpha \cos \beta + \sin \alpha \sin \beta$. For an octopole, the summation is limited to $i, j = 4, 12, 20$, etc. Expression (A4) reduces to Eq. (4) for the ideal multipole case where $i, j = n$ and $a_n = 1$.

Two types of terms in Eq. (A4) may be considered. The terms with $i = j$ represent pure multipoles. Since the effective potentials for higher order multipoles have a radial dependence with higher powers of r, they represent even better approximations to a radial square well than the octopole. Therefore, inclusion of terms of this type can only improve the trapping. The cross terms, where $i \neq j$, have an angular dependence. Such terms produce a "corrugation" in the radial walls of the effective potential. If these terms dominate, ions could slip out the low points in the corrugated wall, reducing the trapping efficiency. Physically, this corresponds to ions which come very close to one of the octopole rods and either collide with it or are deflected out of the trap. However, the higher order terms are important only at large r; the $n = 4$ term dominates in the central region of the octopole. Furthermore, it is always possible to raise the applied voltage sufficiently high that the ions are confined to the central part of the beam guide, say $r < 0.7r_0$, where the angular dependence of the effective field is negligible. In this case, the trapping efficiency remains high, but the actual trapping energy is lower than that given for the ideal case, Eq. (4).

ACKNOWLEDGMENTS

[1] Reaction enthalpies are based on $D_0^0(Ar-H^+) = 3.856 \pm 0.030$ eV [J. Lorenzen, H. Hotop, M.-W. Ruf, and H. Morgner, Z. Phys. A **297**, 19 (1980)], $D_0^0(H_2) = 4.478$ eV, $D_0^0(D_2) = 4.456$ eV, $D_0^0(HD) = 4.514$ eV [K. P. Huber and G. Herzberg, *Constants of Diatomic Molecules* (Van Nostrand Reinhold, New York, 1979)], and tabulated ionization potentials [H. M. Rosenstock, K. Draxl, B. W. Steiner, and J. T. Herron, J. Phys. Chem. Ref. Data **6**, Suppl. 1 (1977)]. Zero-point differences for ArH^+ and ArD^+ are estimated from $\omega_e(ArH^+) = 2723$ cm^{-1} and $\omega_e x_e(ArH^+) = 56$ cm^{-1} [P. Rosmus, Theor. Chim. Acta (Berlin) **51**, 359 (1979)]. Enthalpies given are for the $(^2P_{3/2})$ Ar^+ ground state; those for $(^2P_{1/2})$ Ar^+ are 0.178 eV more exothermic.

[2] D. P. Stevenson and D. O. Schissler, J. Chem. Phys. **29**, 282 (1958).

[3] P. R. Kemper and M. T. Bowers, Int. J. Mass Spectrom. Ion Phys. **52**, 1 (1983).

[4] I. Dotan and W. Lindinger, J. Chem. Phys. **76**, 4972 (1982).

[5] A. B. Rakshit and P. Warneck, J. Chem. Phys. **73**, 2673 (1980); **74**, 2853 (1981).

[6] P. Gaucherel and B. Rowe, Int. J. Mass Spectrom. Ion Phys. **25**, 211 (1977).

[7] W. Lindinger, E. Alge, H. Störi, M. Pahl, and R. N. Varney, J. Chem. Phys. **67**, 3495 (1977).

[8] R. D. Smith, D. L. Smith, and J. H. Futrell, Int. J. Mass Spectrom. Ion Phys. **19**, 395 (1976).

[9] K. R. Ryan and I. G. Graham, J. Chem. Phys. **59**, 4260 (1973).

[10] N. G. Adams, D. K. Bohme, D. B. Dunkin, and F. C. Fehsenfeld, J. Chem. Phys. **52**, 1951 (1970).

[11] M. Henchman, in *Ion–Molecule Reactions*, edited by J. L. Franklin (Plenum, New York, 1972), Vol. 1, pp. 101–259.

[12] F. S. Klein, Proc. Am. Soc. Mass Spectrom., Boston, 1983, p. 97.

[13] Paul F. Fennelly, Ph.D. thesis, Brandeis University, 1972 (University Microfilms, Ann Arbor, Mich., No. 72-32095).

[14] E. Teloy and D. Gerlich, Chem. Phys. **4**, 417 (1974); D. Gerlich, Diplomarbeit, University of Freiburg, Federal Republic of Germany, 1971.

[15] D. Hyatt and K. Lacmann, Z. Naturforsch. Teil A **23**, 2080 (1968).

[16] J. B. Homer, R. S. Lehrle, J. C. Robb, and D. W. Thomas, Adv. Mass Spectrom. **3**, 415 (1966).

[17] A. Henglein, K. Lacmann, and B. Knoll, J. Chem. Phys. **43**, 1048 (1965); A. Henglein, K. Lacmann, and G. Jacobs, Ber. Bunsenges. Phys. Chem. **69**, 279, 286 (1965).

[18] C. F. Giese and W. B. Maier II, J. Chem. Phys. **39**, 739 (1963).

[19] M. Chiang, E. A. Gislason, B. H. Mahan, C. W. Tsao, and A. S. Werner, J. Chem. Phys. **52**, 2698 (1970).

[20] P. M. Hierl, Z. Herman, and R. Wolfgang, J. Chem. Phys. **53**, 660 (1970).

[21] A. Henglein, J. Phys. Chem. **76**, 3883 (1972).

[22] Z. Herman, J. Kerstetter, T. Rose, and R. Wolfgang, Discuss. Faraday Soc. **44**, 123 (1967); Z. Herman and K. Birkenshaw, Ber. Bunsenges. Phys. Chem. **77**, 566 (1973).

[23] L. D. Doverspike, R. L. Champion, and T. L. Bailey, J. Chem. Phys. **45**, 4385 (1966).

[24] A. Henglein and K. Lacmann, Adv. Mass Spectrom. **3**, 331 (1966); A. Henglein, in *Ion–Molecule Reactions in the Gas Phase*, edited by P. J. Ausloos (American Chemical Society, Washington, D.C., 1966), p. 63; A. Ding, K. Lacmann, and A. Henglein, Ber. Bunsenges. Phys. Chem. **71**, 596 (1967).

[25] R. D. Fink and J. S. King, Jr., J. Chem. Phys. **47**, 1857 (1967).

[26] M. A. Berta, B. Y. Ellis, and W. S. Koski, in Ref. 24, p. 80; J. Chem. Phys. **44**, 4612 (1966).

[27] J. H. Futrell and F. P. Abramson, in Ref. 24, p. 107.

[28] F. S. Klein and L. Friedman, J. Chem. Phys. **41**, 1789 (1964).

[29] K. Tanaka, J. Dirup, T. Kato, and I. Koyano, J. Chem. Phys. **74**, 5561 (1981).

[30] W. A. Chupka and M. E. Russell, J. Chem. Phys. **49**, 5426 (1968).

[31] T. Kato, J. Chem. Phys. **80**, 6105 (1984).

[32] P. M. Hierl, V. Pacak, and Z. Herman, J. Chem. Phys. **67**, 2678 (1977).

[33] A. F. Hedrick, T. F. Moran, K. J. McCann, and M. R. Flannery, J. Chem. Phys. **66**, 24 (1977).

[34] T. L. Budzynski and T. L. Bailey, Int. J. Mass Spectrom. Ion Phys. **18**, 317 (1975).

[35] P. Mahadevan and G. D. Magnuson, Phys. Rev. **171**, 103 (1968).

[36] R. C. Amme and J. F. McIlwain, J. Chem. Phys. **45**, 1224 (1966).

[37] E. Gustaffson and E. Lindholm, Ark. Fys. **45**, 1224 (1966).

[38] S. N. Ghosh and W. F. Sheridan, Indian J. Phys. **31**, 337 (1957); J. Chem. Phys. **26**, 480 (1957).

[39] H. B. Gilbody and J. B. Hasted, Proc. R. Soc. London Ser. A **238**, 334 (1956).

[40] F. Wolf, Ann. Phys. **27**, 543 (1936).

[41] G. Gioumousis and D. P. Stevenson, J. Chem. Phys. **29**, 294 (1958).

[42] E. T.-Y. Hsieh and A. W. Castleman, Jr., Int. J. Mass Spectrom. Ion Phys. **40**, 295 (1981).

[43] T. Su and M. T. Bowers, in *Gas Phase Ion Chemistry*, edited by M. T. Bowers (Academic, New York, 1979), Vol. 1, p. 83.

[44] R. D. Smith, D. L. Smith, and J. H. Futrell, Int. J. Mass Spectrom. Ion Phys. **19**, 369 (1976).

[45] B. H. Mahan, J. Chem. Phys. **55**, 1436 (1971); Acc. Chem. Res. **8**, 55 (1975).

[46] S. Chapman and R. K. Preston, J. Chem. Phys. **60**, 650 (1974).

[47] P. J. Kuntz and A. C. Roach, J. Chem. Soc. Faraday Trans. 2 **68**, 259 (1972).

[48] M. Baer and J. A. Beswick, Chem. Phys. Lett. **51**, 360 (1977); Phys. Rev. A **19**, 1559 (1979); M. Baer, Mol. Phys. **35**, 1637 (1978).

[49] P. J. Kuntz, Chem. Phys. Lett. **4**, 129 (1969); P. J. Kuntz and A. C. Roach, J. Chem. Phys. **59**, 6299 (1973).

[50] T. F. George and R. J. Suplinskas, J. Chem. Phys. **54**, 1037, 1046 (1971).

[51] B. H. Mahan, W. E. W. Ruska, and J. S. Winn, J. Chem. Phys. **65**, 3888 (1976).

[52] D. A. Micha and J.-M. Yuan, J. Chem. Phys. **63**, 5462 (1975); J.-M. Yuan and D. A. Micha, *ibid.* **64**, 1032 (1976).

[53] P. M. Hierl, J. Chem. Phys. **67**, 4665 (1977).

[54] (a) K. M. Ervin, S. K. Loh, N. Aristov, and P. B. Armentrout, J. Phys. Chem. **87**, 3593 (1983); (b) P. B. Armentrout, S. K. Loh, and K. M. Ervin, J. Am. Chem. Soc. **106**, 1161 (1984); (c) K. M. Ervin and P. B. Armentrout, J. Chem. Phys. **80**, 2978 (1984); (d) N. Aristov and P. B. Armentrout, J. Am. Chem. Soc. **106**, 4065 (1984); (e) J. L. Elkind and P. B. Armentrout, J. Phys. Chem. **88**, 5454 (1984).

[55] R. A. Yost and D. D. Fetterolf, Mass Spectrom. Rev. **2**, 1 (1983).

[56] W. R. Gentry, in *Gas Phase Ion Chemistry*, edited by M. T. Bowers (Academic, New York, 1979), Vol. 2, p. 221.

[57] D. Smith and N. G. Adams, Ref. 56, Vol. 1, p. 1.

[58] T. A. Lehman and M. M. Bursey, *Ion Cyclotron Resonance Spectrometry* (Wiley–Interscience, New York, 1976).

[59] H. Udseth, C. F. Giese, and W. R. Gentry, Phys. Rev. A **8**, 2483 (1973).

[60] S. G. Hansen, J. M. Farrar, and B. H. Mahan, J. Chem. Phys. **73**, 3750 (1980).

[61] W. R. Gentry, E. A. Gislason, B. H. Mahan, and C.-W. Tsao, J. Chem. Phys. **49**, 3058 (1968).

[62] S. L. Anderson, F. A. Houle, D. Gerlich, and Y. T. Lee, J. Chem. Phys. **75**, 2153 (1981); H. Villinger, J. H. Futrell, A. Saxer, R. Richter, and W. Lindinger, J. Chem. Phys. **80**, 2543 (1984); W. Bustamente, Ph.D. thesis, University of California, Berkeley, 1983.

[63] R. A. Yost and C. B. Enke, Anal. Chem. **51**, 1251A (1979).

[64] L. D. Landau and E. M. Lifshitz, *Mechanics*, 3rd ed. (Oxford, New York, 1976), p. 93; H. G. Dehmelt, in *Advances in Atomic and Molecular Physics*, edited by D. R. Bates (Academic, New York, 1967), Vol. 3, p. 53; see also Ref. 14.

[65] G. Mauclaire, R. Derai, S. Fenistein, and R. Marx, J. Chem. Phys. **70**, 4017 (1979).

[66] G. Loriot and T. Moran, Rev. Sci. Instrum. **46**, 140 (1975).

[67] S. Rosin and I. I. Rabi, Phys. Rev. **48**, 373 (1935); I. Amdur and J. E. Jordon, Adv. Chem. Phys. **10**, 29 (1966).

[68] N. R. Daly, Rev. Sci. Instrum. **31**, 264 (1959).

[69] R. E. Fox, W. H. Hickam, D. J. Grove, and T. Kjeldaas, Jr., Rev. Sci. Instrum. **26**, 1101 (1955).

[70] R. P. Clow and J. H. Futrell, Int. J. Mass Spectrom. Ion Phys. **8**, 119 (1972).

[71] P. J. Chantry, J. Chem. Phys. **55**, 2746 (1971).

[72] L. A. Melton and R. G. Gordon, J. Chem. Phys. **55**, 5449 (1969).

[73] C. Lifshitz, R. L. C. Wu, T. O. Tiernan, and D. T. Terwillger, J. Chem. Phys. **68**, 247 (1978).

[74] For example, P. B. Armentrout, L. F. Halle, and J. L. Beauchamp, J. Chem. Phys. **76**, 2449 (1982).

[75] A. Henglein, in discussion following C. F. Giese, Adv. Mass Spectrom. **3**, 321 (1966).

[76] K. M. Ervin and P. B. Armentrout (to be published).

[77] R. D. Levine and R. B. Bernstin, J. Chem. Phys. **56**, 281 (1972).

[78] The rate constant for reaction (1) from in drift tube studies by Rakshit and Warneck (Ref. 5 and Table I) is for $(^2P_{3/2})$Ar⁺. A very small rate of $k = 7.5 \times 10^{-12}$ was reported for $(^2P_{1/2})$Ar⁺ and an unusually large rate for quenching of the upper spin orbit state by H_2 was obtained ($k_q = 2.2 \times 10^{-9}$). These results are in sharp disagreement with the TESICO state-selected experiments (Ref. 29). The interpretation of the drift tube results is based solely on the measured pressure dependence of Ar⁺ attenuation and is probably in error.

[79] J. O. Hirshfelder, C. R. Curtiss, and R. B. Bird, *Molecular Theory of Gases and Liquids* (Wiley, New York, 1954), p. 947.

[80] J. D. Poll and L. Wolniewicz, J. Chem. Phys. **68**, 3058 (1978).

[81] T. Su and M. T. Bowers, Int. J. Mass. Spectrom. Ion Phys. **17**, 309, 424 (1976).

[82] F. Celli, G. Weddle, and D. P. Ridge, J. Chem. Phys. **73**, 801 (1980).

[83] In particular, coupling between orbital angular momentum and rotational angular momentum is neglected. For a discussion of such coupling for the ion–dipole potential see Ref. 42. In numerical trajectory calculations on a charge-quadrupole potential [J. V. Dugan and R. W. Palmer, Chem. Phys. Lett. **13**, 144 (1972)], it was found that orientation effects depended in a complicated way on the initial impact parameter.

[84] E. A. Gislason, J. Chem. Phys. **57**, 3396 (1972).

[85] B. S. Rabinovitch and D. W. Setser, Adv. Photochem. **3**, 1 (1964).

[86] R. M. Bilotta, F. N. Preuninger, and J. M. Farrar, J. Chem. Phys. **73**, 1637 (1980).

[87] G. Herzberg, *Molecular Spectra and Molecular Structure I. Spectra of Diatomic Molecules*, 2nd ed. (Van Nostrand Reinhold, New York, 1950), p. 426.

[88] K. T. Gillen, B. H. Mahan, and J. S. Winn, J. Chem. Phys. **59**, 6380 (1973).

[89] P. B. Armentrout and J. L. Beauchamp, Chem. Phys. **48**, 315 (1980).

[90] S. A. Safron and G. W. Coppenger, J. Chem. Phys. **80**, 1929, 4907 (1984).

[91] G. Chambaud, B. Levy, and Ph. Millie, Int. J. Quantum Chem. **18**, 49 (1980).

[92] E. G. Jones, R. L. C. Wu, B. M. Hughes, T. O. Tiernan, and D. G. Hopper, J. Chem. Phys. **73**, 5631 (1980).

[93] An excited spectator model was proposed for HD⁺ + rare gas reactions by R. W. Rozett and W. S. Koski, J. Chem. Phys. **49**, 3737 (1968).

[94] D. K. Bohme, J. B. Hasted, and P. P. Ong, Chem. Phys. Lett. **1**, 259 (1967).

[95] T. F. Moran and P. C. Cosby, J. Chem. Phys. **51**, 5724 (1969).

[96] D. R. Denison, J. Vac. Sci. Technol. **8**, 266 (1971).